Earth System
Science
Data

Open Access

Discussions

1 # Marine terraces of the last interglacial period along the Pacific

2 # coast of South America (1°N-40°S)

3 Roland Freisleben[1], Julius Jara-Muñoz[1], Daniel Melnick[2,3], José Miguel Martínez[2,3], Manfred R.
4 Strecker[1]

5 [1] Institut für Geowissenschaften, Universität Potsdam, 14476 Potsdam, Germany
6 [2] Instituto de Ciencias de la Tierra, TAQUACH, Universidad Austral de Chile, Valdivia, Chile
7 [3] Millennium Nucleus The Seismic Cycle Along Subduction Zones, Valdivia, Chile

8 *Correspondence to*: Roland Freisleben (freisleb@uni-potsdam.de)

9 **Abstract.** Tectonically active coasts are dynamic environments characterized by the presence of multiple marine
10 terraces formed by the combined effects of wave-erosion, tectonic uplift, and sea-level oscillations at glacial-cycle
11 timescales. Well-preserved erosional terraces from the last interglacial sea-level highstand are ideal marker horizons
12 for reconstructing past sea-level positions and calculating vertical displacement rates. We carried out an almost
13 continuous mapping of the last interglacial marine terrace along ~5,000 km of the western coast of South America
14 between 1°N and 40°S. We used quantitatively replicable approaches constrained by published terrace-age estimates
15 to ultimately compare elevations and patterns of uplifted terraces with tectonic and climatic parameters in order to
16 evaluate the controlling mechanisms for the formation and preservation of marine terraces, and crustal deformation.
17 Uncertainties were estimated on the basis of measurement errors and the distance from referencing points. Overall,
18 our results indicate a median elevation of 30.1 m, which would imply a median uplift rate of 0.22 m/ka averaged over
19 the past ~125 ka. The patterns of terrace elevation and uplift rate display high-amplitude (~100–200 m) and long-
20 wavelength (~10^2 km) structures at the Manta Peninsula (Ecuador), the San Juan de Marcona area (central Peru), and
21 the Arauco Peninsula (south-central Chile). Medium-wavelength structures occur at the Mejillones Peninsula and
22 Topocalma in Chile, while short-wavelength (< 10 km) features are for instance located near Los Vilos, Valparaíso,
23 and Carranza, Chile. We interpret the long-wavelength deformation to be controlled by deep-seated processes at the
24 plate interface such as the subduction of major bathymetric anomalies like the Nazca and Carnegie ridges. In contrast,
25 short-wavelength deformation may be primarily controlled by sources in the upper plate such as crustal faulting,
26 which, however, may also be associated with the subduction of topographically less pronounced bathymetric
27 anomalies. Latitudinal differences in climate additionally control the formation and preservation of marine terraces.
28 Based on our synopsis we propose that increasing wave height and tidal range result in enhanced erosion and
29 morphologically well-defined marine terraces in south-central Chile. Our study emphasizes the importance of using
30 systematic measurements and uniform, quantitative methodologies to characterize and correctly interpret marine
31 terraces at regional scales, especially if they are used to unravel tectonic and climatic forcing mechanisms of their
32 formation. This database is an integral part of the World Atlas of Last Interglacial Shorelines (WALIS), published
33 online at http://doi.org/10.5281/zenodo.4309748 (Freisleben et al., 2020).

34   **1.   Introduction**

35   Tectonically active coasts are highly dynamic geomorphic environments and they host densely-populated centers and

36   associated infrastructure (Melet et al., 2020). Coastal areas have been episodically affected by the effects of sea-level

37   changes at glacial timescales, drastically modifying the landscape and leaving behind fossil geomorphic markers, such

38   as former paleo-shorelines, abrasion platforms, and marine terraces (Lajoie, 1986). One of the most prominent coastal

39   landforms are marine terraces that were generated during the protracted last interglacial sea-level highstand occurred

40   ~125 ka ago (Siddall et al., 2006). These terraces are characterized by a higher preservation potential, which facilitates

41   their recognition, mapping and lateral correlation. Furthermore, because of their high degree of preservation and

42   relatively young age, they have been used to estimate vertical deformation rates at local and regional scales. The

43   relative abundance and geomorphic characteristics of the last interglacial marine terraces make them ideal geomorphic

44   markers with which to reconstruct past sea-level positions and to enable comparisons between distant sites under

45   different climatic and tectonic settings.

46   The Western South American Coast (WSC) is a tectonically active region that has been repeatedly affected by

47   megathrust earthquakes and associated surface deformation (Beck et al., 1998; Melnick et al., 2006; Bilek, 2010;

48   Baker et al., 2013). Interestingly, previous studies have shown that despite the broad spectrum of latitudinal climatic

49   conditions and erosional regimes along the WSC, marine terraces are scattered, but omnipresent along the coast (Ota

50   et al., 1995; Rehak et al., 2010; Bernhardt et al., 2016; Melnick, 2016; Bernhardt et al., 2017). However, only a few

51   studies on interglacial marine terraces have been conducted along the WSC, primarily in specific areas where they are

52   best expressed; this has resulted in disparate and inconclusive marine terrace measurements based on different

53   methodological approaches and ambiguous interpretations concerning their origin in a tectonic and climatic context

54   (Hsu et al., 1989; Ortlieb and Macharé, 1990; Hsu, 1992; Macharé and Ortlieb, 1992; Pedoja et al., 2006b; Saillard et

55   al., 2009; Regard et al., 2010; Saillard et al., 2011; Rodríguez et al., 2013; Pedoja et al., 2014). This lack of reliable

56   data points has revealed a need to re-examine the last interglacial marine terraces along the WSC based on standardized

57   methodologies in order to obtain a systematic and continuous record of marine terrace elevations along the coast. This

58   information is crucial in order to increase our knowledge of the climatic and tectonic forcing mechanisms that

59   contributed to the formation and degradation of marine terraces in this region.

60   Marine terrace sequences at tectonically active coasts are landforms formed by wave erosion and/or accumulation of

61   sediments resulting from the interaction between tectonic uplift and superposed oscillating sea-level changes (Lajoie,

62   1986; Anderson et al., 1999; Jara-Muñoz et al., 2015). Typically, marine terrace elevations are estimated based on the

63   shoreline angle. The marine terrace morphology comprises a gently inclined marine abrasion platform or depositional

64   surface that terminates landward at a steeply sloping paleo-cliff surface. The intersection point between both surfaces

65   represents the sea-level position during the formation of the marine terrace also known as shoreline angle; if coastal

66   uplift is rapid, such uplifting abrasion or depositional surfaces may be preserved in the landscape and remain unaltered

67   by the effects of subsequent sea-level oscillations (Lajoie, 1986).

Earth System
Science
Data
Open Access
Discussions

68   The analysis of elevation patterns based on shoreline-angle measurements at subduction margins has been largely used

69   to estimate vertical deformation rates and the mechanisms controlling deformation, including the interaction of the

70   upper plate with bathymetric anomalies, the activity of crustal faults in the upper plate, and deep-seated processes

71   such as basal accretion of subducted trench sediments (Taylor et al., 1987; Hsu, 1992; Macharé and Ortlieb, 1992; Ota

72   et al., 1995; Saillard et al., 2011; Pedoja et al., 2014; Jara-Muñoz et al., 2015; Melnick, 2016). The shoreline angle

73   represents a 1D descriptor of the marine terrace elevation, whose measurements are reproducible when using

74   quantitative morphometric approaches (Jara-Muñoz et al., 2016). Furthermore, the estimation of the marine terrace

75   elevations based on shoreline angles can be further improved by quantifying their relationship with paleo-sea level,

76   also known as the indicative meaning (Lorscheid and Rovere, 2019).

77   In this continental-scale compilation of marine terrace elevations along the WSC, we present systematically mapped

78   shoreline angles of marine terraces of the last (Eem/Sangamon) interglacial obtained along 5,000 km of coastline

79   between 1°N and 40°S. In this synthesis we rely on chronological constraints from previous regional studies and

80   compilations (Pedoja et al., 2014). For the first time we are able to introduce an almost continuous pattern of terrace

81   elevation and coastal uplift rates at a spatial scale of 10^3 km along the WSC. Furthermore, in our database we compare

82   tectonic and climatic parameters to elucidate the mechanisms controlling the formation and preservation of marine

83   terraces, and patterns of crustal deformation along the coast. This study was thus primarily intended to provide a

84   comprehensive, standardized database and description of last interglacial marine terrace elevations along the

85   tectonically active coast of South America. This database therefore affords future research into coastal environments

86   to decipher potential tectonic forcings with regard to the deformation and seismotectonic segmentation of the forearc;

87   as such this database will ultimately help to decipher the relationship between upper-plate deformation, vertical motion

88   and bathymetric anomalies and aid in the identification of regional fault motions along pre-existing anisotropies in the

89   South American continental plate. Finally, our database includes information on climate-driving forcing mechanisms

90   that may influence the formation, modification and/or destruction of marine terraces in different climatic sectors along

91   the South American convergent margin. This new database is part of the World Atlas of Last Interglacial Shorelines

92   (WALIS), published online at http://doi.org/10.5281/zenodo.4309748 (Freisleben et al., 2020).

93   **2.   Geologic and geomorphic setting of the WSC**

94   **2.1.   Tectonic and seismotectonic setting**

95   **2.1.1.   Subduction geometry and bathymetric features**

96   The tectonic setting of the convergent margin of South America is controlled by subduction of the oceanic Nazca plate

97   beneath the South American continental plate. The convergence rate varies between 66 mm/a in the north (8°S latitude)

98   and 74 mm/a in the south (27°S latitude) (Fig. 1). The convergence azimuth changes slightly from N81.7° toward

99   N77.5° from north to south (DeMets et al., 2010). The South American subduction zone is divided into four major

100   segments inferred from the spatial distribution of Benioff seismicity (Barazangi and Isacks, 1976; Jordan et al., 1983)

101   (Fig. 1). The segments beneath northern and central Peru (2°–15°S) and beneath central Chile (27°–33°S) are

102   characterized by a gentle dip of the subducting plate between 5° and 10° at depths of ~100 km (Hayes et al., 2018),
103   whereas the segments beneath southern Peru and northern Chile (15°–27°S), and beneath southern Chile (33°–45°S)
104   have steeper dips of 25° to 30°. Spatial distributions of earthquakes furthermore indicate a steep-slab subduction
105   segment in Ecuador and southern Colombia (2°S to 5°N), and a flat-slab segment in NW Colombia (north of 5°N)
106   (Pilger, 1981; Cahill and Isacks, 1992; Gutscher et al., 2000; Ramos and Folguera, 2009). Processes that have been
107   inferred to be responsible for the shallowing of the subduction slab include the subduction of large buoyant ridges or
108   plateaus (Espurt et al., 2008) as well as the combination of trenchward motion of thick, buoyant cratonic lithosphere
109   accompanied by trench retreat (Sobolev and Babeyko, 2005; Manea et al., 2012). Volcanic activity as well as the
110   forearc architecture and distribution of upper-plate deformation further emphasize the location of flat-slab subduction
111   segments (Jordan et al., 1983; Kay et al., 1987; Ramos and Folguera, 2009).

112   Several bathymetric anomalies have been recognized on the subducting Nazca plate. The two most prominent
113   anomalies being subducted beneath South America are the Carnegie and Nazca aseismic ridges at 0° and 15°S,
114   respectively. The Carnegie Ridge subducts roughly parallel with the convergence direction and its position should
115   have remained relatively stable beneath the continent (Angermann et al., 1999; Gutscher et al., 1999; DeMets et al.,
116   2010; Martinod et al., 2016a). In contrast, the obliquity of the Nazca Ridge with respect to the convergence direction
117   resulted in 500 km SE-directed migration of the subduction locus during the last 10 Ma (Hampel, 2002; Saillard et al.,
118   2011; Martinod et al., 2016a). Similarly, smaller aseismic ridges such as the Juan Fernández Ridge and the Iquique
119   Ridge subduct beneath the South American continent at 32°S and 21°S, respectively. The subduction of these
120   bathymetric anomalies are thought to influence the characteristics of interplate coupling and seismic rupture (Bilek et
121   al., 2003; Wang and Bilek, 2011; Geersen et al., 2015; Collot et al., 2017) and mark the boundaries between flat and
122   steep subduction segments and changes between subduction erosion and accretion (Jordan et al., 1983; von Huene et
123   al., 1997; Ramos and Folguera, 2009) (Fig. 1).

124   In addition to bathymetric anomalies, several studies have shown that variations in the amount of sediments in the
125   trench may control the subduction regime from an erosional mode to an accretionary mode (von Huene and Scholl,
126   1991; Bangs and Cande, 1997). In addition, the amount of sediment in the trench has also been hypothesized to
127   influence the style of interplate seismicity (Lamb and Davis, 2003). At the southern Chile margin, thick trench
128   sediments and a steeper subduction angle correlate primarily with subduction accretion, although the area of the
129   intercept of the continental plate with the Chile Rise spreading center locally exhibits the opposite case (von Huene
130   and Scholl, 1991; Bangs and Cande, 1997). Subduction erosion characterizes the region north of the southern volcanic
131   zone from central and northern Chile to southern Peru (33°–15°S) due to decreasing sediment supply to the trench,
132   especially within the flat-slab subduction segments (Stern, 1991; von Huene and Scholl, 1991; Bangs and Cande,
133   1997; Clift and Vannucchi, 2004). Clift and Hartley (2007) and Lohrmann et al. (2003) argued for an alternate style
134   of slow tectonic erosion leading to underplating of subducted material below the base of the crustal forearc,
135   synchronous with tectonic erosion beneath the trenchward part of the forearc. For the northern Andes, several authors
136   also classify the subduction zone as an erosional type (Clift and Vannucchi, 2004; Scholl and Huene, 2007; Marcaillou
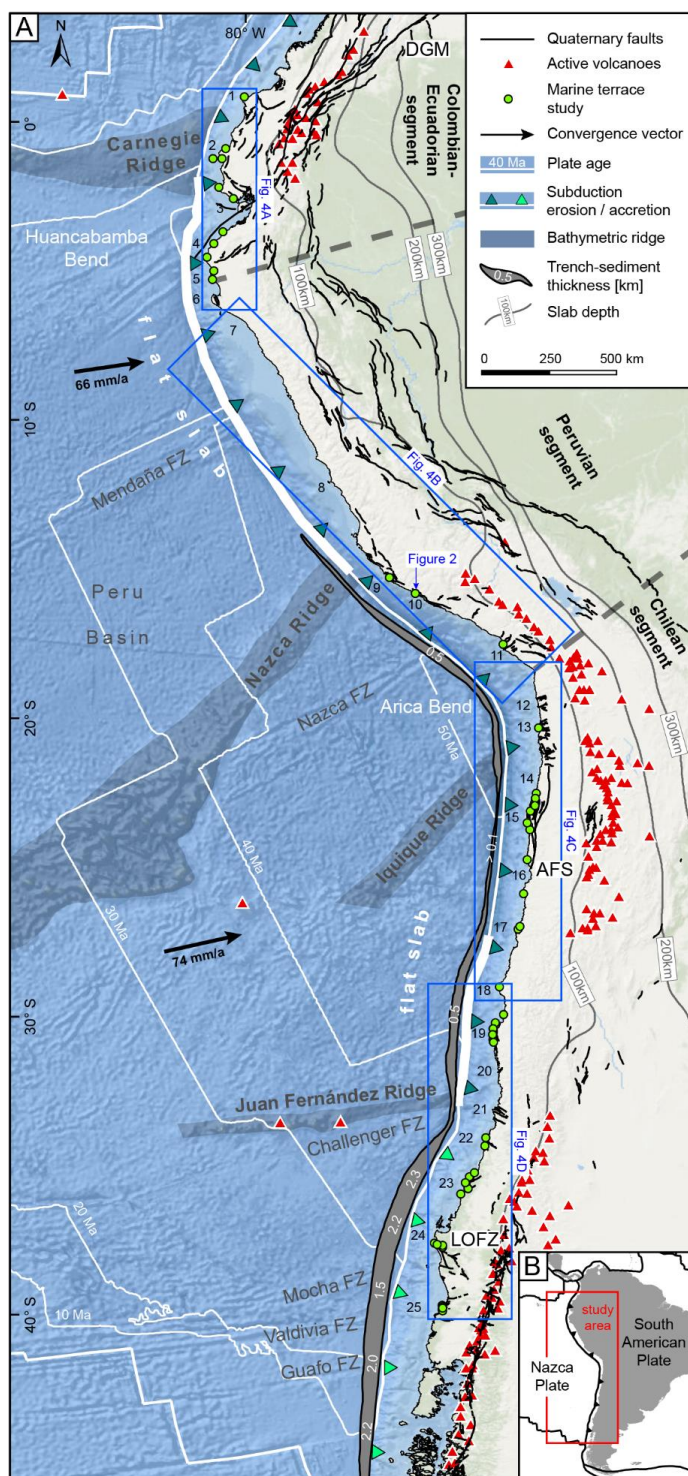137   et al., 2016).

2.1.2. Major continental fault systems in the coastal realm

The South American convergent margin comprises several fault systems with different kinematics. Here we summarize the main structures that affect the Pacific coastal areas. North of the Talara bend (5°S), active thrusting and dextral strike-slip faulting dominates. The most prominent dextral fault in this region is the 2000-km-long, northeast-striking Dolores-Guayaquil megashear (DGM), which starts in the Gulf of Guayaquil and terminates in the Colombian hinterland east of the range-bounding thrust faults of the Colombian Andes (Veloza et al., 2012; Villegas-Lanza et al., 2016) (Fig. 1). The coastal lowlands of Ecuador comprise several thrust faults, while normal faulting in the Gulf of Guayaquil and dextral strike-slip faulting at the Santa Elena Peninsula can be observed farther south (Veloza et al., 2012). Normal faults have been described along the coast of Peru at the Illescas Peninsula in the north (6°S), in the San Juan de Marcona area with the El Huevo–Lomas fault system (14.5°–16°S), and the Incapuquio fault system in the south (17°–18°S) (Veloza et al., 2012; Villegas-Lanza et al., 2016). The main fault zones of the Chilean convergent margin comprise the Atacama Fault System (AFS) in the Coastal Cordillera extending from Iquique to La Serena (29.75°S) with predominantly N-S-striking normal faults, which result in relative uplift of their western side (e.g., Mejillones fault, Salar del Carmen fault) (Naranjo, 1987; González and Carrizo, 2003; Cembrano et al., 2007). Smaller coastal fault systems farther south are located in the Altos de Talinay area (30.5°S, Puerto Aldea fault), near Valparaíso (33°S, Quintay and Valparaíso faults), near the Arauco Peninsula (36°–39°S, Santa María and Lanalhue faults), and in between (Topocalma, Pichilemu, Carranza, and Pelluhue faults) (Ota et al., 1995; Melnick et al., 2009; Santibáñez et al., 2019; Maldonado et al., 2020; Melnick et al., 2020). However, there is still limited knowledge regarding Quaternary slip rates and kinematics and, most importantly, the location of active faults along the forearc region of South America (Jara-Muñoz et al., 2018; Melnick et al., 2019).

2.2. Climate and geomorphic setting

2.2.1. Geomorphology

The 8000-km-long Andean orogen is a major, hemisphere-scale feature that can be divided into different segments with distinctive geomorphic and tectonic characteristics. The principal segments comprise the NNE-SSW trending Colombian-Ecuadorian segment (12°N–5°S), the NW-SE oriented Peruvian segment (5°–18°S), and the N-S trending Chilean segment (18°–56°S) (Jaillard et al., 2000) (Fig. 1). Two major breaks separate these segments; these are the Huancabamba bend in northern Peru and the Arica bend at the Peru-Chile border. The distance of the trench from the WSC coastline averages 118 km and ranges between 44 and 217 km. The depth of the trench fluctuates between 2920 and 8177 m (GEBCO Bathymetric Compilation Group, 2020), and the continental shelf has an average width of 28 km (Paris et al., 2016).

Figure 1. (A) Morphotectonic setting of the South American margin showing major fault systems/crustal faults (Costa et al., 2000; Veloza et al., 2012; Melnick et al., 2020), slab depth (Hayes et al., 2018), and flat-slab subduction segments, active volcanos (Venzke, 2013), bathymetric features of the subducting plate, trench-sediment thickness (Bangs and Cande, 1997), segments of subduction erosion and accretion (Clift and Vannucchi, 2004), plate age (Müller et al., 2008), convergence vectors (DeMets et al., 2010), and marine terrace ages used for lateral correlation. DGM: Dolores-Guayaquil megashear, AFS: Atacama Fault System, LOFZ: Liquiñe-Ofqui Fault Zone, FZ: Fracture Zone, 1: Punta Galera, 2: Manta Pen., 3: Santa Elena Pen., 4: Tablazo Lobitos, 5: Paita Pen., 6: Illescas Pen., 7: Chiclayo, 8: Lima, 9: San Juan de Marcona, 10: Chala Bay, 11: Pampa del Palo, 12: Pisagua, 13: Iquique, 14: Tocopilla, 15: Mejillones Pen., 16: Taltal, 17: Caldera, 18: Punta Choros, 19: Altos de Talinay, 20: Los Vilos, 21: Valparaíso, 22: Topocalma, 23: Carranza, 24: Arauco Pen., 25: Valdivia (World Ocean Basemap: Esri, Garmin, GEBCO, NOAA NGDC, and other contributors). (B) Location of the study area.

168

169   In the 50- to 180-km-wide coastal area of the Ecuadorian Andes, where the Western Cordillera is flanked by a

170   structural depression, relief is relatively low (< 300 m asl). The Gulf of Guayaquil (3°S) and the Dolores-Guayaquil

171   megashear separate the northern from the southern forearc units. The coast-trench distance along the Huancabamba

172   bend is quite small (~55–90 km), except for the Gulf of Guayaquil, and the trench east of the Carnegie Ridge is at a

173   relatively shallow depth of ~3.5 km. Farther south, the Peruvian forearc comprises the up to 160-km-wide Coastal

174   Plains in the north and the narrow, 3000-m-high Western Cordillera. While the Coastal Plains in north-central Peru

175   are relatively narrow (< 40 km), they widen in southern Peru, and the Western Cordillera increases to more than 5000

176   m (Suárez et al., 1983; Jaillard et al., 2000). The region between the coast and the trench in central Peru (up to 220

177   km) narrows toward the San Juan de Marcona area (~75 km) near the Nazca Ridge, and the relatively deep trench

178   (~6.5 km) becomes shallower (< 5 km) (GEBCO Bathymetric Compilation Group, 2020). Between 18°S and 28°S,

179   the Chilean forearc comprises the 50-km-wide and up to 2700-m-high Coastal Cordillera, which is separated from the

180   Precordillera by the Central Depression. In the flat-slab subduction segment between 27°S and 33°S there is neither a

181   morphotectonic region characterized by a central depression nor active volcanism in the high Andean cordillera (Fig.

182   1) (Jordan et al., 1983). The Chilean forearc comprises the Coastal Cordillera, which varies in altitude from up to 2000

183   m at 33°S to 500 m at 46°S, and the Central Depression that separates the forearc from the Main Cordillera. From the

184   Arica bend, where the coast-trench distance is up to 170 km and the trench ~8 km deep, a slight increase in distance

185   can be observed in Chile toward the south (~80–130 km), as can a decrease in trench depth to ~4.5 km.

186   **2.2.2.   Marine terraces and coastal uplift rates**

187   Wave erosion forms wave-cut terrace levels, while the accumulation of shallow marine sediments during sea-level

188   highstands forms wave-built terraces. Another type of terrace is known as "rasa" and refers to wide shore platforms

189   formed under slow-uplift conditions (< 0.2 m/ka), and the repeated reoccupation of this surface by high sea levels

190   (Anderson et al., 1999; Regard et al., 2010; Rodríguez et al., 2013; Melnick, 2016). Typically, the formation of

191   Pleistocene marine terraces in the study area occurred during interglacial and interstadial relative sea-level highstands

192   that were superposed on the uplifting coastal areas; according to the Quaternary oxygen-isotope curve defining warm

193   and cold periods, high Quaternary sea levels have been correlated with warm periods and are denoted with the odd-

194   numbered Marine Isotope Stages (MIS) (Lajoie, 1986; Shackleton et al., 2003).

195   Along the WSC, staircase-like sequences of multiple marine terraces are preserved nearly continuously along the

196   coast. They comprise primarily wave-cut surfaces that are frequently covered by beach ridges of siliciclastic sediments

197   and local accumulations of carbonate bioclastic materials along the beach ridges (Ota et al., 1995; Saillard et al., 2009;

198   Rodríguez et al., 2013; Martinod et al., 2016b). Rasa surfaces exist in the regions of southern Peru and northern Chile

199   (Regard et al., 2010; Rodríguez et al., 2013; Melnick, 2016). Particularly the well-preserved MIS-5e terrace level has

200   been largely used as a strain marker in the correlation of uplifted coastal sectors due to its lateral continuity and high

201   potential for preservation. Global observations of sea-level fluctuations during MIS-5 differentiate between three

202   second-order highstands at 80 ka (5a), 105 ka (5c), and 128 to 116 ka (5e) with paleo-sea levels of -20 m for both of

203   the younger and +3 ± 3 m for the oldest highstand (Stirling et al., 1998; Siddall et al., 2006; Hearty et al., 2007;
204   Rohling et al., 2009; Pedoja et al., 2014). The database generated in this study is based exclusively in the last
205   interglacial marine terraces exposed along the WSC, between Ecuador and Southern Chile (1°S to 40°S). In the
206   following section we present a brief review of previously studied marine terrace sites in this area.

207   Paleo-shoreline elevations of the last interglacial (MIS-5e) in Ecuador are found at elevations of around 45 ± 2 m asl
208   in Punta Galera (Esmeraldas area), 43–57 ± 2 m on the Manta Peninsula and La Plata Island, and 15 ± 5 m asl on the
209   Santa Elena Peninsula (Pedoja et al., 2006b; Pedoja et al., 2006a). In northern Peru, MIS-5e terraces have been
210   described at elevations of 18–31 m asl for the Tablazo Lobitos (Cancas and Mancora areas), at 25 ± 5 m asl on the
211   Paita Peninsula, and at 18 ± 3 m asl on the Illescas Peninsula and the Bay of Bayovar (Pedoja et al., 2006b). Farther
212   south, MIS-5e terraces are exceptionally high in the San Juan de Marcona area immediately south of the subducting
213   Nazca Ridge, with maximum elevations of 80 m at the Cerro Tres Hermanas and 105 m at the Cerro El Huevo (Hsu
214   et al., 1989; Ortlieb and Macharé, 1990; Saillard et al., 2011). The Pampa del Palo region in southern Peru shows
215   relatively thick vertical stacks of shallow marine terrace deposits related to MIS-7, 5e (~20 m), and 5c that may
216   indicate a different geodynamic behavior compared to adjacent regions (Ortlieb et al., 1996). In central and northern
217   Chile, the terrace levels of the last interglacial exist at 250–400 m, 150–240 m, 80–130 m, and 30–40 m, and in
218   southern Chile at 170–200 m, 70 m, 20–38 m, 8–10 m (Fuenzalida et al., 1965). Specifically, between 24°S and 32°S,
219   paleo-shoreline elevations of the last interglacial (MIS-5e) range between 25 and 45 m (Ota et al., 1995; Saillard et
220   al., 2009; Martinod et al., 2016b). Shore platforms are higher in the Altos de Talinay area (30.3°–31.3°S) but are small,
221   poorly preserved, and terminate at a high coastal scarp between 26.75°S and 24°S (Martinod et al., 2016b). Shoreline-
222   angle elevations within the Maule segment (34°–38°S) vary from high altitudes in the Arauco and Topocalma areas
223   (200 m) to moderate elevations near Caranza (110 m) and very low elevations in between (15 m) (Melnick et al., 2009;
224   Jara-Muñoz et al., 2015).

225   Coastal uplift-rate estimates along the WSC mainly comprise calculations for the Talara Arc, the San Juan de Marcona
226   area, the Mejillones Peninsula, the Altos de Talinay area, and several regions in south-central Chile. Along the Talara
227   Arc (6.5°S to 1°N), marine terraces of the Manta Peninsula and La Plata Island in central Ecuador indicate the most
228   extensive uplift rate of 0.31 to 0.42 m/ka, while lower uplift rates are documented to the north in the Esmeraldas area
229   (0.34 m/ka) and especially to the south at the Santa Elena Peninsula (0.1 m/ka). In northern Peru, uplift rates are
230   relative low, ranging from 0.17–0.21 m/ka for the Tablazo Lobitos and 0.16 m/ka for the Paita Peninsula, to 0.12 m/ka
231   for the Bay of Bayovar and the Illescas Peninsula (Pedoja et al., 2006b; Pedoja et al., 2006a). Marine terraces above
232   the subducting Nazca Ridge (13.5°–15.6°S) show variations in uplift rate where the coastal forearc above the northern
233   flank of the ridge is stable or has undergone net subsidence, or where the coast above the ridge crest is rising at about
234   0.3 m/ka and the coast above the southern flank (San Juan de Marcona) is uplifting at a rate of 0.5 m/ka (Hsu, 1992)
235   or at even 0.7 m/ka for at least the last 125 ka according to Ortlieb and Macharé (1990). Saillard et al. (2011) state
236   that long-term regional uplift in the San Juan de Marcona area has increased since about 800 ka related to the
237   southward migration of the Nazca Ridge, and ranges from 0.44 to 0.87 m/ka. The Pampa del Palo area in southern
238   Peru rose more slowly or was even down-faulted and had subsided with respect to the adjacent coastal regions (Ortlieb

239   et al., 1996). These movements ceased after the highstand during the MIS-5e and slow uplift rates of around 0.16 m/ka

240   characterized the region since 100 ka (Ortlieb et al., 1996). In northern Chile (24°–32°S), uplift rates for the Late

241   Pleistocene average around 0.28 ± 0.15 m/ka (Martinod et al., 2016b), except for the Altos de Talinay area, where

242   pulses of rapid uplift occurred during the Middle Pleistocene (Ota et al., 1995; Saillard et al., 2009; Martinod et al.,

243   2016b). The Central Andean rasa (15°–33°S) and the oldest Pleistocene shore platforms – which are also generally

244   wider – indicate accelerated and spatially continuous uplift after a period of tectonic stability or subsidence. According

245   to Melnick (2016), the Central Andean rasa has experienced slow and steady long-term uplift at 0.13 ± 0.04 m/ka

246   during the Quaternary, predominantly accumulating strain through deep earthquakes at the crust-mantle boundary

247   (Moho) below the locked portion of the plate interface. The lowest uplift rates occur at the Arica bend and increase

248   gradually southward; the highest values are reached along geomorphically distinct peninsulas (Melnick, 2016). In the

249   Maule segment, the mean uplift rate for the MIS-5 terrace level is 0.5 m/ka, exceeded only in the areas of Topocalma,

250   Carranza, and Arauco (reaching up to 1.6 m/ka) (Melnick et al., 2009; Jara-Muñoz et al., 2015). Although there are

251   several studies of marine terraces along the WSC, these are isolated and based on different methodological approaches,

252   mapping and leveling resolution, as well as dating techniques, which makes regional comparisons and correlations

253   difficult.

2.2.3.   Climate

255   Apart from latitudinal temperature changes, the present-day morphotectonic provinces along the South American

256   margin have a pronounced impact on the precipitation gradients on the west coast of South America. Since mountain

257   ranges are oriented approximately perpendicular to moisture-bearing winds, they affect both flanks of the orogen

258   (Strecker et al., 2007). The regional-scale pattern of wind circulation is dominated by westerly winds at

259   subtropical/extratropical latitudes primarily up to about 27°S (Garreaud, 2009). However, anticyclones over the South

260   Pacific result in winds blowing from the south along the coast between 35°S and 10°S (Garreaud, 2009). The moisture

261   in the equatorial Andes (Ecuador and Colombia) and in the areas farther south (27°S) is fed by winds from the Amazon

262   basin and the Gulf of Panama, resulting in rainfall mainly on the eastern flanks of the mountain range (Bendix et al.,

263   2006; Bookhagen and Strecker, 2008; Garreaud, 2009). The Andes of southern Ecuador, Peru, and northern Chile are

264   dominated by a rain-shadow effect that causes aridity within the Andean Plateau (Altiplano-Puna), the Western

265   Cordillera, and the coastal region (Houston and Hartley, 2003; Strecker et al., 2007; Garreaud, 2009). Furthermore,

266   the aridity is exacerbated by the effects of the cold Humboldt current, which prevents humidity from the Pacific from

267   penetrating inland (Houston and Hartley, 2003; Garreaud, 2009; Coudurier-Curveur et al., 2015). The precipitation

268   gradient reverses between 27°S and 35°S, where the Southern Hemisphere Westerlies cause abundant rainfall on the

269   western flanks of the Coastal and Main cordilleras (Strecker et al., 2007; Garreaud, 2009). Martinod et al. (2016b) has

270   proposed that latitudinal differences in climate largely influence coastal morphology, specifically the formation of

271   high coastal scarps that prevent the development of extensive marine terrace sequences. However, the details of this

272   relationship have not been conclusively studied along the full extent of the Pacific coast of South America.

3. Methods

273

274 We combined – and describe in detail below – bibliographic information, different topographic data sets, and uniform
275 morphometric and statistical approaches to assess the elevation of marine terraces and accompanying vertical
276 deformation rates along the South American margin.

3.1. Mapping marine terraces

277

278 Marine terraces are primarily described based on their elevation, which is essential for determining vertical
279 deformation rates. The measurements of the marine terrace elevations of the last interglacial were performed using
280 TanDEM-X topography (12 and 30 m horizontal resolution) (German Aerospace Center (DLR), 2018), and digital
281 terrain models from LiDAR (1, 2.5, and 5 m horizontal resolution). The DEMs were converted to orthometric heights
282 using the ellipsoid projection of the World Geodetic System (WGS1984) and the EGM2008 (E_{EGM08}) geoid. The
283 orthometrically corrected DEMs were projected in Universal Transverse Mercator (UTM) projections of varying
284 zones, namely WGS84 UTM Zone 19S for Chile, Zone 18S for southern/central Peru, and Zone 17S for northern
285 Peru/Ecuador.

286 To trace the MIS-5 shoreline, we mapped its inner edge along the west coast of South America based on the TanDEM-
287 X topography (Fig. 2A). To facilitate mapping, we used slope and hillshade maps. We correlated the inner edge
288 mapping with the marine terraces catalog of Pedoja et al. (2014) and the references therein (section 2.2.2, Table 1).
289 Further references used to validate MIS-5e terrace heights include Victor et al. (2011) for the Pampa de Mejillones,
290 Martinod et al. (2016b) for northern Chile, and Jara-Muñoz et al. (2015) for the area between 34° and 38°S. The
291 referencing point with the nearest distance to the location of our measurements served as an orientation for the MIS-
292 5 terrace elevation in the respective area.

293 A rigorous assessment of marine terrace elevations is crucial for determining accurate vertical deformation rates. Since
294 fluvial degradation and hillslope processes after the abandonment of marine terraces may alter their morphology
295 (Anderson et al., 1999; Jara-Muñoz et al., 2015), direct measurements of terrace elevations at the inner edge (foot of
296 the paleo-cliff) may result in overestimation of the terrace elevations and vertical deformation rates (Jara-Muñoz et
297 al., 2015). To precisely measure the shoreline-angle elevations of the MIS-5 terrace level, we used a profile-based
298 approach in TerraceM, a graphical user interface in MATLAB® (Jara-Muñoz et al., 2016), available at
299 www.terrace.com. We placed swath profiles of variable width perpendicular to the previously mapped inner edge,
300 which were used by the TerraceM algorithm to extract maximum elevations to avoid fluvial incision (Fig. 2A). North
301 of Caleta Chañaral (29°S), we used swath profiles of 200 m width, although we occasionally used 100-m-wide profiles
302 for narrow terrace remnants. South of 29°S, we used swath widths of 130 and 70 m. The width was chosen based on
303 fluvial drainage densities that are associated with climate gradients. Sensitivity tests comparing shoreline-angle
304 measurements from different swath widths in the Chala Bay show only minimal deviations of less than 0.5 m (Fig.
305 2C). The sections of these profiles, which represent the undisturbed paleo-platform and paleo-cliff, were picked
306 manually and fitted by linear regression. The extrapolated intersection between both regression lines ultimately

307   determines the buried shoreline-angle elevation and associated uncertainty, which is derived from the 95% confidence

308   interval (2σ) of both regressions (Fig. 2B). In total, we measured 1843 and 110 shoreline-angle elevations of the MIS-

309   5e and MIS-5c terrace levels, respectively. To quantify the paleo-position of the relative sea-level elevation and the

310   involved uncertainty for the WALIS template, we calculated the indicative meaning using the IMCalc software from

311   Lorscheid and Rovere (2019).

312
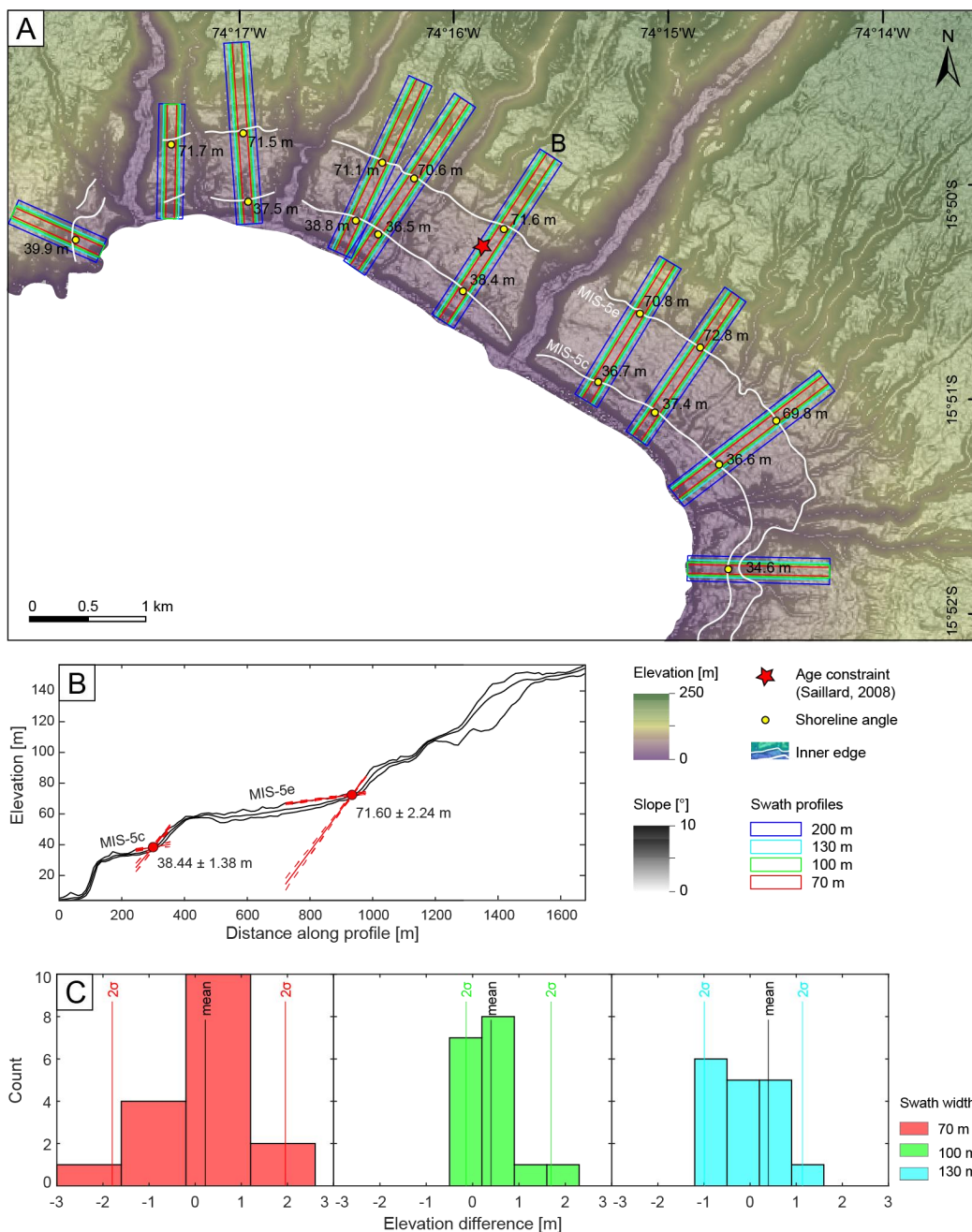
Figure 2. (A) Orthometrically corrected TanDEM-X and slope map of Chala Bay in south-central Peru with mapped
shoreline inner edges of the MIS-5e and 5c terrace levels. Colored rectangles represent swath-profile boxes of various widths
that were placed perpendicular to the inner edges for the subsequent estimation of terrace elevation in TerraceM. The red
star indicates the age constraint for this area (Saillard, 2008). **(B)** Estimation of the shoreline-angle elevation in TerraceM
by intersecting linear-regression fits of the paleo-cliff and paleo-platform. **(C)** Histograms of elevation differences measured
for various swath widths (70 m, 100 m, and 130 m) with respect to the 200-m-wide reference swath profile (blue).

319 **Table 1. Age constraints used for mapping of the inner edge of MIS-5 and for verifying our terrace-elevation measurements.**
320 **This compilation is mainly based on the terrace catalog of Pedoja et al. (2014); added references include Victor et al. (2011)**
321 **for Pampa de Mejillones, Martinod et al. (2016b) for northern Chile, and Jara-Muñoz et al. (2015) for south-central Chile.**
322 **IRSL: Infrared Stimulated Luminescence, AAR: Amino-Acid Racemization, CRN: Cosmogenic Radionuclides, ESR:**
323 **Electron Spin Resonance.**

Country	Location	Latitude	Longitude	Dating method	Confidence	Reference
Ecuador	Galera	0.81	-80.03	IRSL	5	Pedoja et al., 2006
Ecuador	Manta	-0.93	-80.66	IRSL, U/Th	5	Pedoja et al., 2006
Ecuador	La Plata	-1.26	-81.07	U/Th	5	Pedoja et al., 2006
Ecuador	Manta	-1.27	-80.78	IRSL	5	Pedoja et al., 2006
Ecuador	Santa Elena	-2.21	-80.88	U/Th	5	Pedoja et al., 2006
Ecuador	Puna	-2.60	-80.40	U/Th	5	Pedoja et al., 2006
Peru	Cancas	-3.72	-80.75	Morphostratigraphy	5	Pedoja et al., 2006
Peru	Mancora/Lobitos	-4.10	-81.05	Morphostratigraphy	5	Pedoja et al., 2006
Peru	Talara	-4.56	-81.28	Morphostratigraphy	5	Pedoja et al., 2006
Peru	Paita	-5.03	-81.06	Morphostratigraphy	5	Pedoja et al., 2006
Peru	Bayovar/Illescas	-5.31	-81.10	IRSL	5	Pedoja et al., 2006
Peru	Cerro Huevo	-15.31	-75.17	CRN	5	Saillard et al., 2011
Peru	Chala Bay	-15.85	-74.31	CRN	5	Saillard, 2008
Peru	Ilo	-17.55	-71.37	AAR	5	Ortlieb et al., 1996b; Hsu et al., 1989
Chile	Punta Lobos	-20.35	-70.18	U/Th, ESR	5	Radtke, 1989
Chile	Cobija	-22.55	-70.26	Morphostratigraphy	4	Ortlieb et al., 1995
Chile	Michilla	-22.71	-70.28	AAR	3	Leonard & Wehmiller, 1991
Chile	Hornitos	-22.85	-70.30	U/Th	5	Ortlieb et al., 1996
Chile	Chacaya	-22.95	-70.30	AAR	5	Ortlieb et al., 1996
Chile	Pampa Mejillones	-23.14	-70.45	U/Th	5	Victor et al., 2011
Chile	SW Mejillones/Punta Jorge	-23.54	-70.55	U/Th, ESR	3	Radtke, 1989
Chile	Coloso	-23.76	-70.46	ESR	3	Schellmann & Radtke, 1997
Chile	Punta Piedras	-24.76	-70.55	CRN	5	Martinod et al., 2016
Chile	Esmeralda	-25.91	-70.67	CRN	5	Martinod et al., 2016
Chile	Caldera	-27.01	-70.81	U/Th, ESR	5	Marquardt et al., 2004
Chile	Bahia Inglesa	-27.10	-70.85	U/Th, ESR	5	Marquardt et al., 2004
Chile	Caleta Chanaral	-29.03	-71.49	CRN	5	Martinod et al., 2016
Chile	Coquimbo	-29.96	-71.34	AAR	5	Leonard & Wehmiller, 1992; Hsu et al., 1989
Chile	Punta Lengua de Vaca	-30.24	-71.63	U/Th	5	Saillard et al., 2012
Chile	Punta Lengua de Vaca	-30.30	-71.61	U/Th	5	Saillard et al., 2012
Chile	Quebrada Palo Cortado	-30.44	-71.69	CRN	5	Saillard et al., 2009
Chile	Rio Limari	-30.63	-71.71	CRN	5	Saillard et al., 2009
Chile	Quebrada de la Mula	-30.79	-71.70	CRN	5	Saillard et al., 2009
Chile	Quebrada del Teniente	-30.89	-71.68	CRN	5	Saillard et al., 2009
Chile	Puertecillo	-34.09	-71.94	IRSL	5	Jara-Munoz et al., 2015
Chile	Pichilemu	-34.38	-71.97	IRSL	5	Jara-Munoz et al., 2015
Chile	Putu	-35.16	-72.25	IRSL	5	Jara-Munoz et al., 2015
Chile	Constitucion	-35.40	-72.49	IRSL	5	Jara-Munoz et al., 2015
Chile	Constitucion	-35.44	-72.47	IRSL	5	Jara-Munoz et al., 2015
Chile	Carranza	-35.58	-72.61	IRSL	5	Jara-Munoz et al., 2015
Chile	Carranza	-35.64	-72.54	IRSL	5	Jara-Munoz et al., 2015
Chile	Pelluhue	-35.80	-72.54	IRSL	5	Jara-Munoz et al., 2015
Chile	Pelluhue	-35.80	-72.55	IRSL	5	Jara-Munoz et al., 2015
Chile	Curanipe	-35.97	-72.78	IRSL	5	Jara-Munoz et al., 2015
Chile	Arauco	-37.62	-73.67	IRSL	5	Jara-Munoz et al., 2015
Chile	Arauco	-37.68	-73.57	CRN	5	Melnick et al., 2009
Chile	Arauco	-37.71	-73.39	CRN	5	Melnick et al., 2009
Chile	Arauco	-37.76	-73.38	CRN	5	Melnick et al., 2009
Chile	Cerro Caleta Curi–anco	-39.72	-73.40	Tephrochronology	4	Pino et al., 2002
Chile	South Curi–anco	-39.76	-73.39	Tephrochronology	4	Pino et al., 2002
Chile	Valdivia	-39.80	-73.39	Tephrochronology	4	Pino et al., 2002
Chile	Camping Bellavista	-39.85	-73.40	Tephrochronology	4	Pino et al., 2002
Chile	Mancera	-39.89	-73.39	Tephrochronology	5	Silva, 2005

324

325 To quantify the reliability and consistency of our shoreline-angle measurements, we applied a quality rating from low

326 (1) to high (5) confidence. The four parameters that are included in our quality rating (QR) comprise a) the distance

327 to the nearest referencing point (D_{RP}), b) the confidence of the referencing point that is based on the dating method

328 used by previous studies (C_{RP}) (Pedoja et al., 2014), c) the measurement error in TerraceM (E_T), and (d) the pixel-

329 scale resolution of the topographic data set (R) (Fig. 3). We did not include the error that results from the usage of

330 different swath widths, since the calculated elevation difference with respect to the most frequently used 200 m swath

331 width is very low (< 0.5 m) (Fig. 2C). From the reference points we only used data points with a confidence value of

332 3 or greater (1 – poor, 5 – very good) based on the previous qualification of Pedoja et al. (2014). We further used this

333 confidence value to quantify the quality of the age constraints in the WALIS template. To account for the different

334 uncertainties of the individual parameters in the QR, we combined and weighted the parameters D_{RP} and C_{RP} in a first

335 equation claiming 60% of the final QR, E_T in a second and R in a third equation weighted 30% and 10%, respectively.
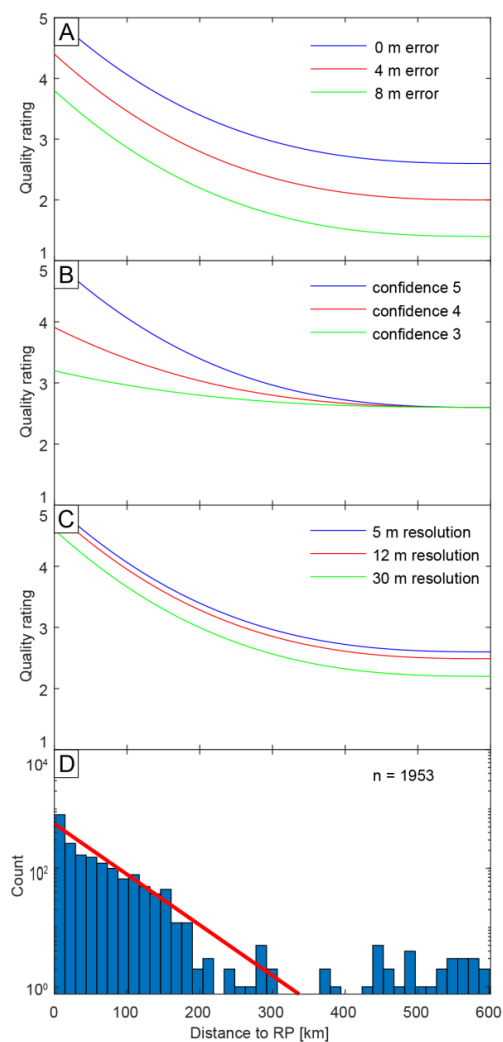
Figure 3. Influence of the parameters on the quality rating. The y-axis is the distance to reference point (RP), x-axis is the quality rating, the color lines represent different values of quality rating parameters. While one parameter is being tested, the remaining parameters are set to their best values. That is why the QR does not reach values of 1 in the graphs displayed here. (A) Shoreline-angle elevation error. (B) Confidence value of the referencing point. (C) Topographic resolution of the DEM used for terrace-elevation estimation. (D) Histogram displaying the distribution of distances between each shoreline-angle measurement and its nearest RP (n: number of measurements). The red line is an exponential fit.

337 We justify these percentages by the fact that the distance and confidence to the nearest referencing point is of utmost

338 importance for identifying the MIS-5e terrace level. The measurement error represents how well the mapping of the

339 paleo-platform and paleo-cliff led to the shoreline-angle measurement, while the topographic resolution of the

340 underlying DEM only influences the precise representation of the actual topography and has little impact on

341 measurement itself. Furthermore, we added an exponent to the first part of the equation to reinforce low confidence

342 and/or high distance of the referencing point for low quality ratings. The following equation illustrates how we

343 calculated the individual parameters and the overall quality rating:

344
$$QR = 1 + 2.4 * \left(\frac{C_{RP}}{\max(C_{RP})} * \left(1 - \frac{D_{RP}}{\max(D_{RP})}\right) \right)^e + 1.2 * \left(1 - \frac{E_T}{\max(E_T)}\right) + 0.4 * 1.2 * \left(1 - \frac{R}{\max(R)}\right)$$

345 The influence of each parameter to the quality rating can be observed in Fig. 3. We observe that for high D_{RP} values

346 the QR becomes constant; likewise, the influence of QR parameters becomes significant for QR values higher than 3.

347 We justify the constancy of the QR for high D_{RP} values (> 300 km) by the fact that most terrace measurements have

348 D_{RP} values below 200 km (Fig. 3D). The quality rating is then used as a descriptor of the confidence of marine terrace-

349 elevation measurements.

350 **3.2.   Estimating coastal uplift rates**

351 Uplift-rate estimates from marine terraces *(u)* were calculated using the following equations:

352
$$\Delta H = H_T - H_{SL}$$

353
$$u = \frac{H_T - H_{SL}}{T}$$

354 where *ΔH* is the relative sea level, H_{SL} is the sea-level altitude of the interglacial maximum, H_T is the shoreline-angle

355 elevation of the marine terrace, and *T* its associated age (Lajoie, 1986).

356 We calculated the standard error *SE(u)* using the following equation from Gallen et al. (2014):

357
$$SE(u)^2 = u^2 \left(\left(\frac{\sigma_{\Delta H}^2}{\Delta H^2}\right) + \left(\frac{\sigma_T^2}{T^2}\right) \right)$$

358 where $\sigma_{\Delta H}^2$, the error in relative sea level, equals ($\sigma_{H_T}^2 + \sigma_{H_{SL}}^2$). The standard-error estimates comprise the uncertainty

359 in shoreline-angle elevations from TerraceM (σ_{H_T}), error estimates in absolute sea level ($\sigma_{H_{SL}}$) from Rohling et al.

360 (2009), and an arbitrary range of 10 ka for the duration of the highstand (σ_T).

361 **3.3.   Tectonic parameters of the South American convergent margin**

362 We compared the deformation patterns of marine terraces along the coast of South America with proxies that included

363 crustal faults, bathymetric anomalies, trench-sediment thickness, and distance to the trench. To evaluate the possible

364   control of climatic parameters in the morphology of marine terraces, we compared our data set with wave heights,

365   tidal range, mean annual precipitation rate, and the azimuth of the coastline (Schweller et al., 1981; Bangs and Cande,

366   1997; von Huene et al., 1997; Collot et al., 2002; Ceccherini et al., 2015; Hayes et al., 2018; Santibáñez et al., 2019;

367   GEBCO Bathymetric Compilation Group, 2020) (Fig. 1).

368   To evaluate the potential correlations between tectonic parameters and marine terraces, we then analyzed the

369   latitudinal variability of these parameters projected along a curved "simple profile" and a 300-km-wide "swath profile"

370   following the trace of the trench. We used simple profiles for visualizing 2D data sets; for instance, to compare crustal

371   faults along the forearc area of the margin (Veloza et al., 2012; Melnick et al., 2020), we projected the seaward tip of

372   each fault. For the trench-sediment thickness, we projected discrete thickness estimates based on measurements from

373   reflection-seismic profiles of Bangs and Cande (1997), Collot et al. (2002), Huene et al. (1996), and Schweller et al.

374   (1981). Finally, we projected the discrete trench distances from the point locations of our marine terrace measurements

375   along a simple profile. To compare bathymetric features on the oceanic plate, we used a compilation of bathymetric

376   measurements at 450 m resolution (GEBCO Bathymetric Compilation Group, 2020). The data set was projected along

377   a curved 300-km-wide swath profile using TopoToolbox (Schwanghart and Kuhn, 2010).

378   Finally, to elucidate the influence of climatic factors on marine terrace morphology, we compared the elevation, but

379   also the number of measurements as a proxy for preservation and exposure of marine terraces. We calculated wave

380   heights, tidal ranges, and reference water levels at the point locations of our marine terrace measurements using the

381   Indicative Meaning Calculator (IMCalc) from Lorscheid and Rovere (2019). We used the maximum values of the

382   hourly significant wave height, and for the tidal range we calculated the difference between the highest and lowest

383   astronomical tide. The reference water level represents the averaged position of the paleo sea level with respect to the

384   shoreline-angle elevation and, together with the indicative range (uncertainty), quantifies the indicative meaning

385   (Lorscheid and Rovere, 2019). We furthermore used the high-resolution data set of Ceccherini et al. (2015) for mean

386   annual precipitation, and we compared the azimuth of the coast in order to evaluate its exposure to wind and waves.

387   To facilitate these comparisons, we extracted the values of all these parameters at the point locations of our marine

388   terrace measurements and project them along a simple profile. Calculations and outputs were processed and elaborated

389   using MATLAB® 2020b.

390   **4.   Results**

391   **4.1.   Marine terrace geomorphology and shoreline-angle elevations**

392   In the following sections we describe our synthesized database of last interglacial marine terrace elevations along the

393   WSC. Marine terraces of the last interglacial are generally well preserved and almost continuously exposed along the

394   WSC, allowing to estimate elevations with a high spatial density. To facilitate the descriptions of marine terrace-

395   elevation patterns, we divided the coastline into four sectors based on their main morphometric characteristics (Fig.

396   4): 1) the Talara bend in northern Peru and Ecuador, 2) southern and central Peru, 3) northern Chile, and 4) central

397   and south-central Chile. In total we carried out 1,843 MIS-5e terrace measurements with a median elevation of 30.1

398 m asl and 110 MIS-5c terrace measurements with a median of 38.6 m. The regions with exceptionally high marine

399 terrace elevations (≥ 100 m) comprise the Manta Peninsula in Ecuador, the San Juan de Marcona area in south-central

400 Peru, and three regions in south-central Chile (Topocalma, Carranza, and Arauco). Marine terraces at high altitudes

401 (≥ 60 m) can also be found in Chile on the Mejillones Peninsula, south of Los Vilos, near Valparaíso, in Tirua, and

402 near Valdivia, while terrace levels only slightly above the median elevation are located at Punta Galera in Ecuador,

403 south of Puerto Flamenco, at Caldera/Bahía Inglesa, near Caleta Chañaral, and near the Quebrada El Moray in the

404 Altos de Talinay area in Chile. In the next sections we described the characteristics of each site in detail, the names of

405 the sites are written in brackets following the same nomenclature as in the WALIS database.

406
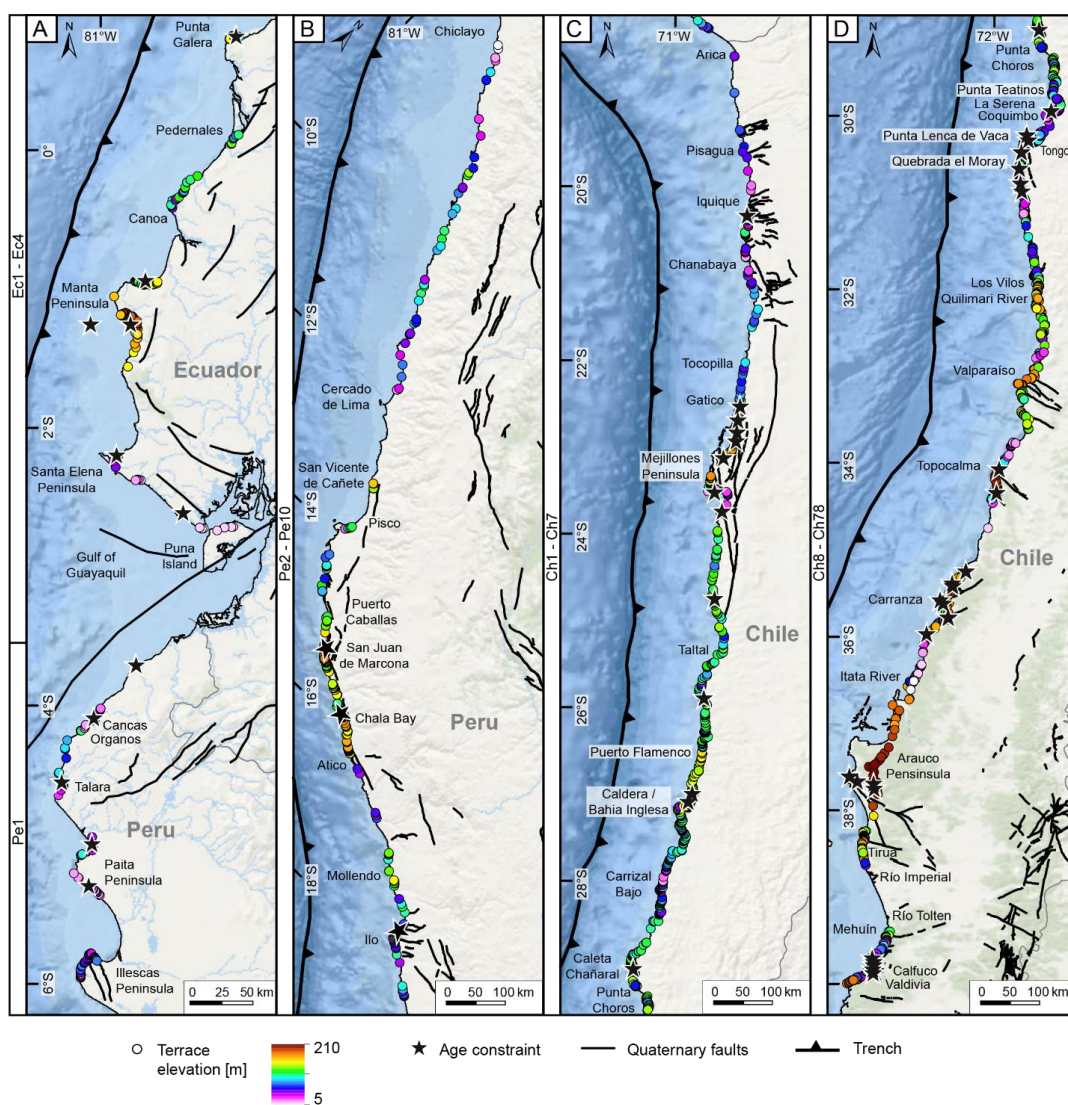
407 **Figure 4. Shoreline-angle elevation measurements (colored points), referencing points (black stars), Quaternary faults (bold**
408 **black lines) (Veloza et al., 2012; Melnick et al., 2020), and locations mentioned in the text for the four main morphometric**
409 **segments (for location see Fig. 1A) (World Ocean Basemap: Esri, Garmin, GEBCO, NOAA NGDC, and other contributors).**
410 **(A) Talara bend in Ecuador and northern Peru. (B) Central and southern Peru. (C) Northern Chile. (D) Central and south-**
411 **central Chile.**

412 ### 4.1.1.   Ecuador and northern Peru (1°N–6.5°S)

413 The MIS-5e terrace levels in Ecuador and northern Peru [sites Ec1 to Ec4 and Pe1] are discontinuously preserved

414 along the coast (Fig. 5). They often occur at low elevations (between 12 m and 30 m) and show abrupt local changes

415 in elevation, reaching a maximum at the Manta Peninsula. Punta Galera in northern Ecuador displays relatively broad

416 and well-preserved marine terraces ranging between 40 and 45 m elevation and rapidly decreasing eastward to around

417 30 m asl across the Cumilínche fault [Ec1]. Farther south, between Pedernales and Canoa [Ec1], narrow terraces occur

418 at lower altitudes of 22–34 m asl. A long-wavelength (~120 km) pattern in terrace-elevation change can be observed

419 across the Manta Peninsula with the highest MIS-5e terraces peaking at ~100 m asl at its southern coast [Ec2]. This

420 terrace level is hardly visible in its highest areas with platform widths smaller than 100 m due to deeply incised and

421 narrowly spaced river valleys. We observe lower and variable elevations between 30 and 50 m across the Rio Salado

422 fault in the San Mateo paleo-gulf in the north, while the terrace elevations increase gradually from ~40 m in the Pile

423 paleo-gulf in the south [Ec3] toward the center of the peninsula (El Aromo dome) and the Montecristi fault [Ec3]. A

424 lower terrace level correlated to MIS-5c displays similar elevation patterns as MIS-5e within the Pile paleo-gulf and

425 northward. Near the Gulf of Guayaquil and the Dolores-Guayaquil megashear, the lowest terrace elevations occur at

426 the Santa Elena Peninsula ranging between 17 and 24 m asl and even lower altitudes in its southern part, and on the

427 Puna Island ranging between 11 and 16 m asl [Ec4]. In northern Peru [Pe1], we observe dismembered MIS-5e terraces

428 in the coastal area between Cancas and Talara below the prominent Mancora Tablazo. "Tablazo" is a local descriptive

429 name used in northern Peru (~3.5–6.5°S) for marine terraces that cover a particularly wide surface area (Pedoja et al.,

430 2006b). South of Cancas, MIS-5e terrace elevations range between 17 and 20 m asl, reaching 32 m near Organos, and

431 vary between 20 and 29 m in the vicinity of Talara. In the southward continuation of the Talara harbor, the Talara

432 Tablazo widens, with a lower marine terrace at around 23 m asl immediately north of Paita Peninsula reaching 30 m

433 asl in the northern part of the peninsula. The last occurrence of well-preserved MIS-5e terraces in this sector is at the

434 Illescas Peninsula, where terrace elevations decrease from around 30 m to 17 m asl southward.
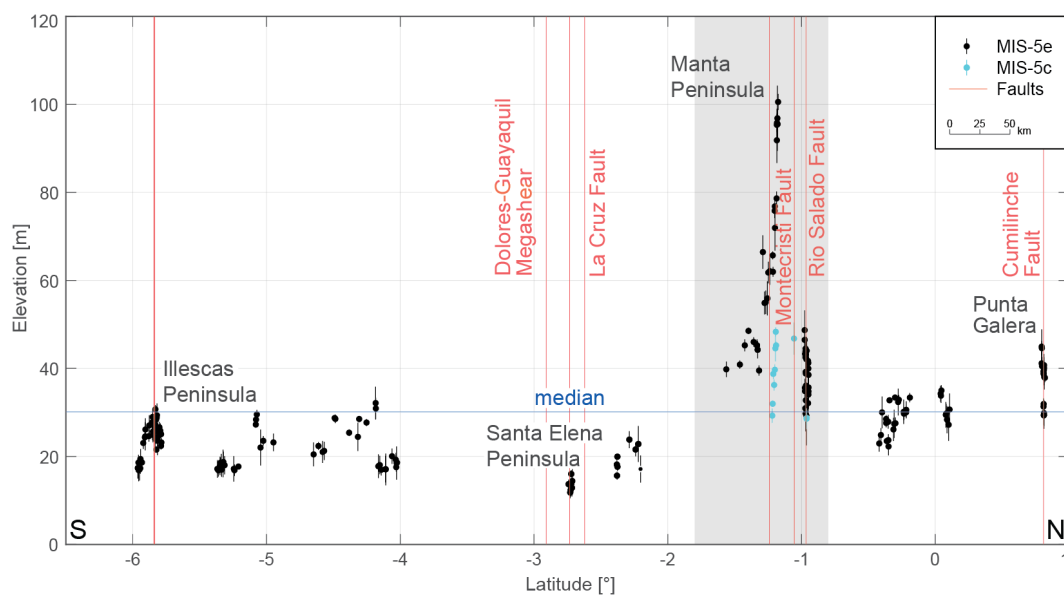
Figure 5. Measured shoreline-angle elevations of MIS-5e and 5c in Ecuador and northern Peru. A high and inferred long-wavelength change in terrace elevation occurs at the Manta Peninsula (gray area) and quite low altitudes farther south at the Santa Elena Peninsula. Several short-scale terrace-elevation changes coincide with faulting at Punta Galera and on the Illescas Peninsula. Median elevation: 30.1 m. For location see Fig. 4A.
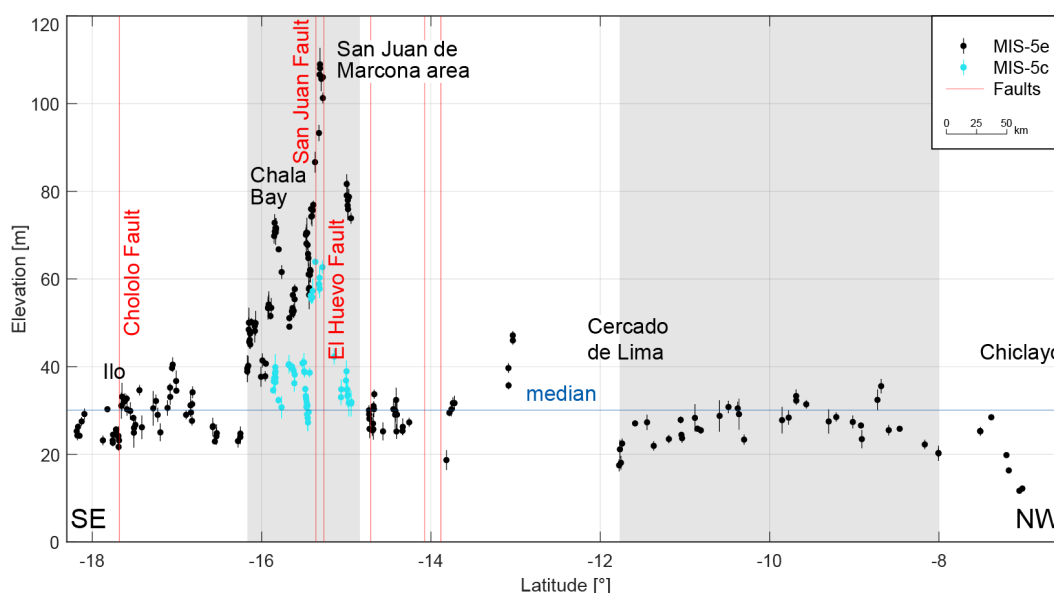
4.1.2.   Central and southern Peru (6.5°–18.3°S)

This segment comprises marine terraces at relatively low and constant elevations, but which are rather discontinuous [sites Pe2 to Pe10], except in the San Juan de Marcona area, where the terraces increase in elevation drastically (Fig. 6). The coast in north-central Peru exhibits poor records of MIS-5e marine terraces, characterized by mostly narrow and discontinuous remnants that are sparsely distributed along the margin. Marine terraces increase in elevation from 11 to 35 m asl south of Chiclayo [Pe2] and decrease to 17 m asl near Cercado de Lima [Pe3, Pe4], forming a long-wavelength (~600 km), small amplitude (~20 m) upwarped structure. The MIS-5e terrace levels are better expressed in the south-central and southern part of Peru at elevations between 35 and 47 m asl in San Vicente de Cañete, decreasing to approximately 30 m asl in the vicinity of Pisco [Pe5]. South of Pisco, the coastal area becomes narrow with terrace elevations ranging between 25 and 34 m asl [Pe6] and increasing abruptly to 74–79 m near Puerto Caballas and the Río Grande delta. MIS-5e terrace elevations are highest within the San Juan de Marcona area, reaching 109–93 m at Cerro Huevo and 87–56 m at Cerro Trés Hermanas [Pe7]. These higher terrace elevations coincide with a wider coastal area, a better-preserved terrace sequence, and several crustal faults, such as the San Juan and El Huevo faults.

Terrace heights west of Yauca indicate a further decrease to 50–58 m before a renewed increase to 70–72 m can be observed in the Chala embayment [Pe8]. We observe a similar trend in elevation changes for the shoreline angles attributed to the MIS-5c interglacial within the previously described high-elevation area: 31–39 m near the Río Grande delta, 62–58 m below the Cerro Huevo peak, 64–27 m below the Cerro Trés Hermanas peak [Pe7], 36–40 m near

458 Yauca, and 34–40 m within the Chala embayment [Pe8]. Besides various changes in between, terrace elevations

459 decrease slowly from 54 m south of the Chala region to 38 m near Atico [Pe8]. The overall decrease south of the San

460 Juan de Marcona area therefore contrasts strikingly with the sharper decrease to the north. These high-elevation marine

461 terraces, which extend ~250 km along the coast from north of the San Juan de Marcona area to south of Chala Bay,

462 constitute one of the longest wavelength structures of the WSC. Southeast of Atico, less well-preserved marine terraces

463 appear again in form of small remnants in a narrower coastal area. Starting with elevations as low as 24 m, MIS-5e

464 terrace altitudes increase southeastward to up to 40 m near Mollendo [Pe9], before they slightly decrease again. The

465 broader and quite well-preserved terraces of the adjacent Ilo area resulted in a smooth increase from values greater

466 than 25 m to 33 m and a sudden decrease to as low as 22 m across the Chololo fault [Pe9]. North of the Arica bend,

467 shoreline-angle measurements yielded estimates of 24–29 m in altitude [Pe10].

468
469 **Figure 6. Measured shoreline-angle elevations of MIS-5e and 5c terraces in central and southern Peru. While only sparsely**
470 **preserved terraces below the median (30.1 m) occur in central Peru between Chiclayo and Lima, a relatively broad and**
471 **asymmetric distribution of marine terraces characterizes the area of San Juan de Marcona. For location see Fig. 4B.**

472 **4.1.3.   Northern Chile (18.3°–29.3°S)**

473 Along the northern Chilean coast, marine terraces of the MIS-5e are characterized by a variable elevation pattern and

474 the occurrence of numerous crustal faults associated with the Atacama fault system, although the changes in terrace

475 elevation are not as pronounced as in the northern segments (Fig. 7) [sites Ch1 to Ch7]. The local widening of the

476 coastal area near the Arica bend narrows southward with MIS-5e terraces at elevations of between 24 and 28 m asl in

477 northernmost Chile [Ch1]. Just north of Pisagua, we measured shoreline-angle elevations of well-preserved marine

478 terraces between 19 and 26 m across the Atajana fault [Ch1]. A short-scale zigzag pattern starting with shoreline-

479 angle elevation values of 32 m south of Iquique and south of the Zofri and Cavancha faults decreases rapidly to

480 approximately 22 m, increases again to similar altitudes and drops as low as 18 m toward Chanabaya south of the

481 Barranco Alto fault [Ch1]. A gentle, steady rise in terrace elevations can be observed south of Tocopilla where
482 altitudes of 25 m are attained. South of Gatico, terrace markers of the MIS-5e highstand increase and continue
483 northward for much of the Mejillones Peninsula within an approximate elevation range of 32–50 m asl, before reaching
484 a maximum of 62 m asl at the Pampa de Mejillones [Ch2]. With its ~100 km latitudinal extent, we consider this
485 terrace-elevation change to be a medium-wavelength structure. Although no MIS-5e terrace levels have been
486 preserved at the Morro Mejillones Horst (Binnie et al., 2016), we measured shoreline-angle elevations at the elevated
487 southwestern part of the peninsula that decrease sharply from 55 to 17 m asl in the vicinity of the Mejillones fault
488 system [Ch2]. After a short discontinuation of the MIS-5e terrace level at Pampa Aeropuerto, elevations remain
489 relatively low between 19–25 m farther south [Ch2]. Along the ~300-km coastal stretch south of Mejillones, marine
490 terraces are scattered along the narrow coastal area ranging between 25 and 37 m asl [Ch3]. South of Puerto Flamenco,
491 MIS-5e terrace elevations range between 40 and 45 m asl until Caldera and Bahía Inglesa [Ch4]. The MIS-5e marine
492 terrace elevations decrease abruptly south of the Caldera fault and the Morro Copiapó (Morro Copiapó fault) to
493 between 25 and 33 m asl, reaching 20 m asl north of Carrizal Bajo [Ch4]. In the southernmost part of the northern
494 Chilean sector, the MIS-5e terraces rise from around 30 m asl to a maximum of 45 m asl near the Cabo Leones fault
495 [Ch4], before declining abruptly near Caleta Chañaral and Punta Choros [Ch5, Ch6, Ch7].
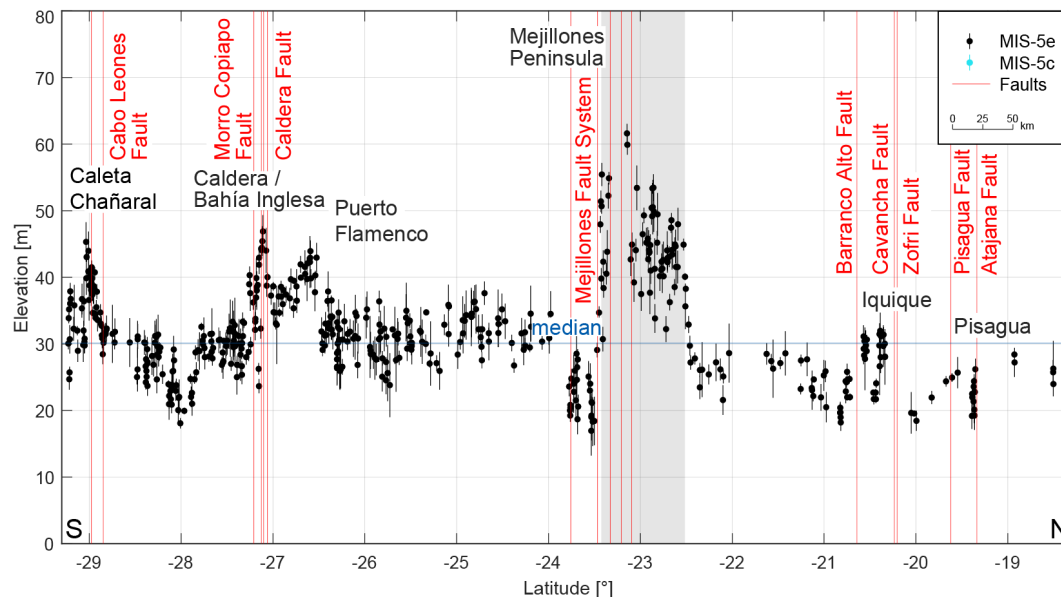
496
497 **Figure 7. Measured shoreline-angle elevations of MIS-5e and 5c terraces in northern Chile. Faults as well as asymmetrically**
498 **uplifted marine terraces of up to 60 m elevation characterize the Mejillones Peninsula, reaching values below 20 m at the**
499 **southern margin. Terrace elevations attain peak values south of Puerto Flamenco, at Caldera/Bahía Inglesa, and north of**
500 **Caleta Chañaral, while in between minimum altitudes below 20 m occur (north of Carizal Bajo). Median elevation is 30.1**
501 **m. For location see Fig. 4C.**

502 **4.1.4.   Central Chile (29.3°–40°S)**

503 Marine terraces along central Chile display variable, high-amplitude terrace-elevation patterns associated with
504 numerous crustal faults, and include a broad-scale change in terrace altitudes with the highest MIS-5e marine terrace

505   elevations of the entire South American margin on the Arauco Peninsula (Fig. 8) [sites Ch8 to Ch78]. South of Punta
506   Choros, marine terrace elevations decrease from values close to 40 to 22 m asl north of Punta Teatinos [Ch8, Ch9]. A
507   maximum elevation of 40 m is reached by the terraces just south of this area [Ch10] whereas north of La Serena, a
508   sharp decrease leads to values between 20 and 30 m for marine terraces south of Coquimbo Bay and in the Tongoy
509   Bay area [Ch11, Ch12]. South of Punta Lengua de Vaca, our measurements of the exceptionally well-preserved
510   staircase terraces are in the same elevation range between 20 and 30 m, increasing slowly to 40 m near the Quebrada
511   el Moray [Ch13]. Although we could not observe a significant change in terrace elevation across the Puerto Aldea
512   fault, we measured an offset of ~7 m across the Quebrada Palo Cortado fault. MIS-5e terrace levels decrease thereafter
513   and vary between 20 and 30 m in altitude until north of Los Vilos [Ch14–Ch18], where they increase in elevation
514   [Ch19], reaching 60 m near the Rio Quilimari [Ch20]. The marine terraces become wider in this area and are associated
515   with scattered sea stacks. Decreasing farther south to only 20 m asl [Ch21–Ch25], the coastal area narrows and has
516   terrace heights of up to 64 m near Valparaíso that are cut by numerous faults (e.g., Valparaíso and Quintay faults)
517   [Ch26–Ch32]. Another low-elevation area follows southward, with values as low as 17 m [Ch33–Ch35]. Farther south,
518   between 34°S and 38°S, broad (~200 km at Arauco), medium (~45 km at Topocalma), and narrow (Carranza)
519   upwarped zones occur that are manifested by variable terrace elevations. These include prominent high-terrace
520   elevations at Topocalma with a maximum of 180 m [Ch36–Ch39], slightly lower levels of 110 m at Carranza [Ch42–
521   Ch47], exceptionally low values near the Río Itata (< 10 m) [Ch48–Ch64, Ch66], and the most extensive and highest
522   shoreline-angle elevations on the Arauco Peninsula with elevations in excess of 200 m [Ch67–Ch73]. Additionally,
523   we measured MIS-5c terrace elevations in the three higher exposed areas with a range of 20–55 m at Carranzo, and a
524   few locations at Topocalma (76–81 m) and Arauco (117–123 m). The medium-wavelength structure of Topocalma is
525   bounded by the Pichilemu and Topocalma faults, and near Carranza several fault offsets (e.g., Pelluhue and Carranza
526   faults) are responsible for the short-wavelength changes in terrace elevation. In contrast, crustal faulting is nearly
527   absent in the high-elevation and long-wavelength structure at Arauco. MIS-5e terrace elevations are highly variable
528   within a short area south of the Arauco Peninsula near the Tirua fault, increasing rapidly from 27 m to 78 m and
529   decreasing thereafter to around 20 m [Ch74, Ch75]. The continuity of terraces is interrupted by the absence of terrace
530   levels between Río Imperial and Río Toltén, but resumes afterward with a highly frequent zigzag pattern and multiple
531   faults (e.g., Estero Ralicura and Curinanco faults) from as low as 18 m to a maximum of 40 m [Ch76, Ch77]. In this
532   area locations with the highest terrace levels comprise the terraces near Mehuín and Calfuco. A final increase in
533   shoreline-angle elevations from around 20–30 m up to 76 m near Valdivia coincides with the southern terminus of our
534   terrace-elevation measurements [Ch78].
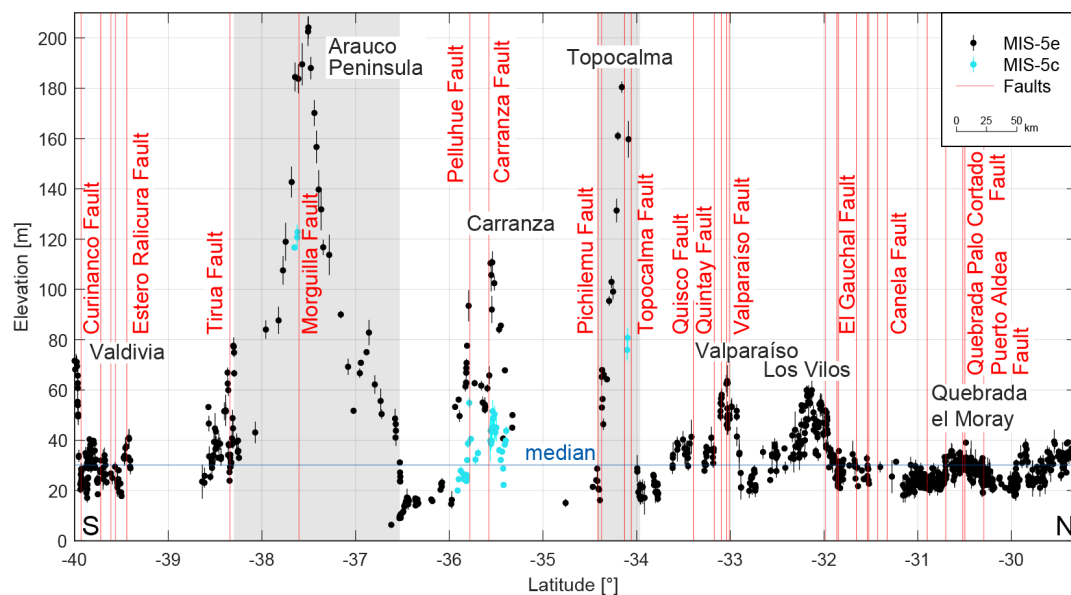
Figure 8. Measured shoreline-angle elevations of MIS-5e and 5c terraces in central Chile. Extensive faulting coincides with various high terrace elevations of the last interglacial highstand north of Los Vilos, near Valparaiso, at Topocalma, Carranza, and near Valdivia. The most pronounced and long-wavelength change in terrace elevation occurs on the Arauco Peninsula with maximum elevations over 200 m and minimum elevations below 10 m north of Concepción. Median elevation: 30.1 m. For location see Fig. 4D.

4.2.   Statistical analysis

Our statistical analysis of mapped shoreline-angle elevations resulted in a maximum kernel density at 28.96 m with a 95% confidence interval from 18.59 m to 67.85 m (2σ) for the MIS-5e terrace level (Fig. 9A). The MIS-5c terrace yielded in a maximum kernel density at a higher elevation of 37.20 m with 2σ ranging from 24.50 m to 63.92 m. It is important to note that the number of MIS-5c measurements is neither as high nor as continuous as compared to that of the MIS-5e level. MIS-5c data points were measured almost exclusively in sites where MIS-5e reach high elevations (e.g., San Juan de Marcona with MIS-5e elevations between 40 and 110 m).

The distribution of measurement errors was studied using probability kernel-density plots for each topographic resolution (1-5 m LIDAR, 12 m TanDEM-X, and 30 m TanDEM-X). The three data sets display similar distributions and maximum likelihood probabilities (MLP); for instance, LiDAR data show a MLP of 0.93 m, the 12 m TanDEM-X a MLP of 1.16 m, and 30 m TanDEM-X a MLP of 0.91 m (Fig. 9B). We observe the lowest errors from the 30 m TanDEM-X, slightly higher errors from the 1-5 m LiDAR data, and the highest errors from the 12 m TanDEM-X. This observation is counterintuitive as we would expect lower errors for topographic data sets with higher resolution. The reason for these errors is probably related to the higher number of measurements using the 12 m TanDEM-X (1564) in comparison with the measurements using 30 m TanDEM-X (50), which result in a higher dispersion (Fig. 9B). In addition, the relation between terrace elevations and error estimates shows that comparatively higher errors are associated with higher terrace elevations, although the sparse point density of high terrace-elevation measurements prevents a clear correlation from being recognized (Fig. 9C).
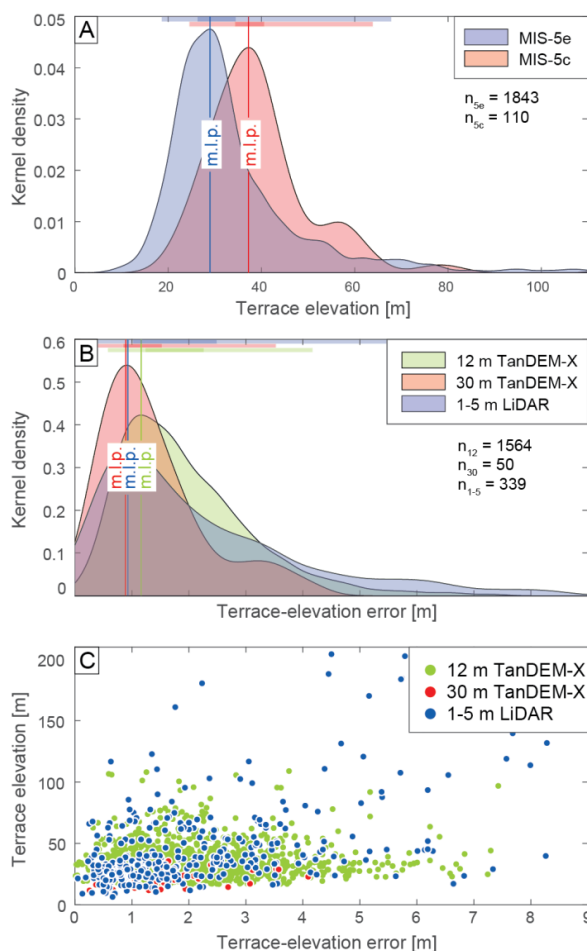
Figure 9. Statistical analysis of measured shoreline-angle elevations. (A) Kernel-density plot of MIS-5e and 5c terrace elevations with maximum likelihood probabilities (MLP.) at 28.96 m elevation for MIS-5e and 37.20 m elevation for MIS-5c (n: number of measurements). Colored bars on top highlight the standard deviations σ and 2σ. (B) Kernel-density and their associated standard-deviation (σ and 2σ) calculations of terrace-elevation errors for source DEMs of various resolutions. The most abundant 12 m TanDEM-X has a MLP-error of 1.16 m, while the 30 m TanDEM-X and the 1-5 m LIDAR produce slightly lower errors of 0.91 m and 0.93 m, respectively. (C) Terrace-elevation errors plotted against terrace elevation for the individual source DEMs. Although the point density for high terrace elevations is low, a weak correlation of high errors with high terrace elevations can be observed.

4.3. Coastal uplift-rate estimates

We calculated uplift rates from 1953 terrace-elevation measurements of MIS-5e (1843) and MIS-5c (110) along the South American margin with a median uplift rate of approximately 0.22 m/ka (Fig. 10). As with the distribution of terrace elevations, we similarly observed several short-scale and long-scale high-amplitude changes in uplift rate along the coast. The most pronounced long-wavelength highs (≥ 1° latitude) in uplift rate are located on the Manta Peninsula (0.79 m/ka), in the San Juan de Marcona area (0.85 m/ka), and on the Arauco Peninsula (1.62 m/ka). Medium-wavelength structures include the Mejillones Peninsula (0.47 m/ka) and Topocalma (1.43 m/ka), while shorter wavelength structures that are characterized by exceptionally high uplift rates seem to be limited to the central Chilean part of the coastline, especially between 31.5° and 40°S. The most striking example includes Carranza with an uplift rate of up to 0.87 m/ka since the formation of the oldest MIS-5 terrace levels. Lower, but still quite high, uplift rates were calculated for areas north of Los Vilos (0.46 m/ka), near Valparaíso (0.49 m/ka), and near Valdivia (0.59 m/ka). The lowest uplift rates along the South American margin occur at Penco immediately north of Concepción (0.03

571   m/ka), south of Chiclayo in northern Peru (0.07 m/ka), and on the southern Santa Elena Peninsula in Ecuador (0.07

572   m/ka).

573   **5.   Discussion**

574   **5.1.   Advantages and limitations of the database of last interglacial marine terrace elevations along the WSC**

575   In this study we generated a systematic database of last interglacial marine terrace elevations with unprecedented

576   resolution based on an almost continuous mapping of ~2,000 measurements along 5,000 km of the WSC. This opens

577   up several possibilities for future applications in which this database can be used; for example, the fact that marine

578   terraces are excellent strain markers used in studies on deformation processes at regional scale, comparisons between

579   deformation rates at different temporal scales or analyses linking specific climate-driven coastal processes, landscape

580   evolution and tectonics. However, there are a number of limitations and potential uncertainties that can affect the use

581   of this database in such studies without taking several caveats into consideration.

582   One of the most critical limitations of using the database is associated with the referencing points used to tie our

583   marine terrace measurements, which are in turn based on the results and chronological constraints provided by

584   previous studies. The referencing points are heterogeneously distributed along the WSC, resulting in some cases of

585   up to 600 km distance to the nearest constrained point, such as in Central Peru [e.g. Pe2]. This may have a strong

586   influence on the confidence in the measurement of the marine terrace elevation at these sites. In addition, the

587   geochronological control of some of the referencing points may be based on dating methods with pronounced

588   uncertainties (e.g., amino acid racemization, electron spin resonance, cosmogenic radionuclides), which may result in

589   equivocal interpretations and chronologies of marine terrace levels. In order to address these potential factors of

590   uncertainty we defined a quality rating (see section 3.1.), which allows classifying our mapping results based on their

591   confidence and reliability. Therefore, by considering measurements above a defined quality it is possible to increase

592   the confidence level of future studies using this database; however, this might result in a decrease of the number of

593   measurement points available for analysis and comparison.

594   **5.2.   Tectonic and climatic controls on the elevation and morphology of marine terraces along the WSC**

595   In this section we provide a brief synthesis of our data set and its implications for coastal processes and overall

596   landscape evolution that are driven by a combination of tectonic and climatic characteristics. This synthesis

597   emphasizes the significance of our comprehensive data set for a variety of coastal research problems that were briefly

598   introduced in section 5.1. Our detailed measurements of marine terraces along the WCS reveal variable elevations and

599   a heterogeneous distribution of uplift rates associated with patterns of short-, medium-, and long-wavelengths. In

600   addition, we observe different degrees of development of marine terraces along the margin expressed in variable

601   shoreline-angle density. There are several possible causes for this variability, which we explore by comparing terrace-

602   elevation patterns with different climatic and tectonic parameters.

603   **5.2.1.   Tectonic controls on coastal uplift rates**

604 The spatial distribution of the MIS-5 marine terrace elevations along the convergent South American margin has
605 revealed several high-amplitude and long-wavelength changes with respect to tectonically controlled topography.
606 Long-wavelength patterns in terrace elevation (~10^2 km) are observed at the Manta Peninsula in Ecuador, central Peru
607 between Chiclayo and Lima, San Juan de Marcona (Peru), and on the Arauco Peninsula in Chile, while medium-
608 wavelength structures occur at Mejillones Peninsula and Topocalma (Chile). Instead, short-wavelength patterns in
609 MIS-5 terrace elevations are observed for instance near Los Vilos, Valparaíso, and Carranza in Chile.

610 The subduction of bathymetric anomalies has been shown to exert a substantial influence on upper-plate deformation
611 (Fryer and Smoot, 1985; Taylor et al., 1987; Macharé and Ortlieb, 1992; Cloos and Shreve, 1996; Gardner et al., 2013;
612 Wang and Bilek, 2014; Ruh et al., 2016), resulting in temporally and spatially variable fault activity, kinematics, and
613 deformation rates (Mann et al., 1998; Saillard et al., 2011; Morgan and Bangs, 2017; Melnick et al., 2019). When
614 comparing the uplift pattern of MIS-5 marine terraces and the bathymetry of the oceanic plate, we observe that the
615 two long-wavelength structures in this area, on the Manta Peninsula and in the San Juan de Marcona, both coincide
616 with the location of the subducting Nazca and Carnegie ridges, respectively (Fig. 10A and B); this was also previously
617 observed by other authors (Gutscher et al., 1999; Pedoja et al., 2006a; Saillard et al., 2011). In summary, long-
618 wavelength structures at the coast may be associated with deep-seated processes (Melosh and Raefsky, 1980; Watts
619 and Daly, 1981) possibly related to changes in the mechanical behavior of the plate interface. In this context it is
620 interesting that the high uplift rates on the Arauco Peninsula do not correlate with bathymetric anomalies, which may
621 suggest a different deformation mechanism. The scarcity of crustal faults described in the Arauco area rather suggests
622 that shallow structures associated with crustal bending and splay-faults occasionally breaching through the upper crust
623 (Melnick et al., 2012; Jara-Muñoz et al., 2015; Jara-Muñoz et al., 2017; Melnick et al., 2019) cause long-wavelength
624 warping and uplift there (Fig. 10A).

625 In contrast, small-scale bathymetric anomalies correlate in part with the presence of crustal faults perpendicular to the
626 coastal margin near, for instance, the Juan Fernandez, Taltal, and Copiapó ridges (Fig. 10B), which result in short
627 wavelength structures and a more localized differentiation of uplifted terraces. This emphasizes also the importance
628 of last interglacial marine terraces with respect to currently active faults, which might be compared in the future with
629 short-term deformation estimates from GPS or the earthquake catalog. In summary, short-wavelength structures may
630 be associated with crustal faults that root at shallower depths within the crust (Jara-Muñoz et al., 2015; Jara-Muñoz et
631 al., 2017; Melnick et al., 2019).

632 The thickness of sediment in the trench is an additional controlling factor on forearc architecture that may determine
633 which areas of the continental margin are subjected to subduction erosion or accretion (Hilde, 1983; Cloos and Shreve,
634 1988; Menant et al., 2020). Our data shows that the accretionary part of the WSC (south of the intersection with the
635 Juan Fernandez Ridge at 32.9°S) displays faster median uplift rates of 0.26 m/ka than in the rest of the WSC (Fig. 10B
636 and C). However, no clear correlation is observed between trench fill, uplift rates, and the different structural patterns
637 in the erosive part of the margin. On the other hand, we observe lower uplift rates for greater distances from the trench
638 at the Arica bend, in central Peru, and in the Gulf of Guayaquil, while higher uplift rates occur in areas closer to the
639 trench, such as near the Nazca and Carnegie ridges and the Mejillones Peninsula.

640   **5.2.2.   Climatic controls on the formation and preservation of last interglacial marine terraces**

641   The latitudinal climate differences that characterize the western margin of South America may also control coastal

642   morphology and the generation and preservation of marine terraces (Martinod et al., 2016b). In order to evaluate the

643   influence of climate in the generation and/or degradation of marine terraces, we compared the number of marine

644   terrace measurements, which is a proxy for the degree of marine terrace preservation, and climatically controlled

645   parameters such as wave height, tidal range, coastline orientation, and the amount of precipitation.

646   The maximum wave height along the coast of South America decreases northward from ~8 to ~2 m (see section 3.3,

647   Fig. 10D). Similarly, the tidal range decreases progressively northward from 2 to 1 m between Valdivia and San Juan

648   de Marcona, followed by a rapid increase to 4 m between San Juan de Marcona and the Manta Peninsula. We observe

649   an apparent correlation between the number of measurements and the tidal range in the north, between Illescas and

650   Manta (Fig. 10F). Likewise, the increasing trend in the number of measurements southward matches with the increase

651   in wave height (Fig. 10D). An increase of wave height and tidal range may lead to enhanced erosion and

652   morphologically well-expressed marine terraces, which is consequently reflected in a higher number of measurements.

653   Furthermore, we observe low values for the reference water level (< 0.7 m) resulting from tide and wave-height

654   estimations in IMCalc (Lorscheid and Rovere, 2019), which are used to correct our shoreline-angle measurements

655   (see section 3.3.).

656   The control of wave-erosion processes on the morphological expression of marine terraces may be counteracted by

657   erosional processes such as river incision. We note that the high number of preserved marine terraces between

658   Mejillones and Valparaíso decreases southward, which coincides with a sharp increase in mean annual precipitation

659   from 10 to 1000 mm/yr (Fig. 10E and F). However, in the area with a high number of measurement points between

660   the Illescas Peninsula and Manta we observe an opposite correlation: higher rainfall associated with an increase of

661   marine terrace preservation (Fig. 10E). This anticorrelation suggests that the interplay between marine terrace

662   generation and degradation processes apparently buffer each other, resulting in different responses under different

663   climatic conditions and coastal settings.

664   The higher number of marine terraces between Mejillones and Valparaíso and north of Illescas corresponds with a

665   SSW-NNE orientation of the coastline (azimuth between 200 and 220°). In contrast, NW-SE to N-S oriented coastlines

666   (azimuth between 125 and 180°), such as between the Arica and Huancabamba bends, correlate with a lower number

667   of marine terrace measurements (Fig. 10E and F). This observation is, however, counterintuitive considering that NW-

668   SE oriented coastlines may be exposed more directly to the erosive effect of storm waves associated with winds

669   approaching from the south. We interpret the orientation of the coastline therefore to be of secondary importance at

670   regional-scale for the formation of marine terraces compared to other parameters, such as wave height, tidal range, or

671   rainfall.
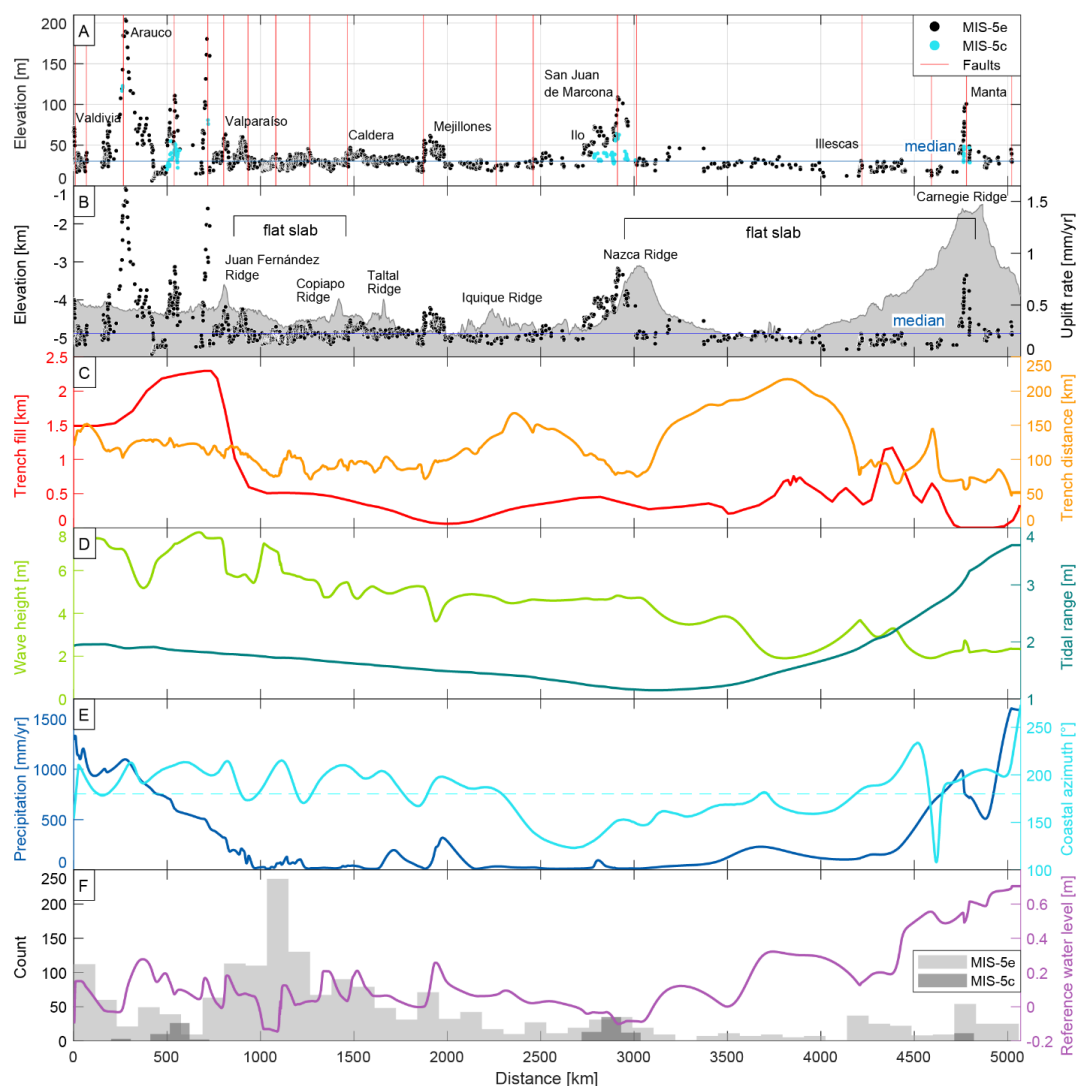
672
673 **Figure 10. Terrace-elevation and uplift-rate estimates plotted in comparison with various parameters (i.e., bathymetry,**
674 **trench fill, trench distance, wave height, tidal range, precipitation, and coastal azimuth) that might influence the disparate**
675 **characteristics of our marine terrace distribution that has been revealed by our data set. We projected these parameters,**
676 **elevations, and uplift rates to a S-N-oriented polyline that represents the trench. (A) Terrace-elevation measurements and**
677 **most important crustal faults (Veloza et al., 2012; Melnick et al., 2020). This shows the range of altitudes in different regions**
678 **along the coast and possible relationships to crustal faulting. The blue horizontal line indicates the median elevation (30.1**
679 **m). (B) Coastal uplift rates and mean bathymetry (GEBCO Bathymetric Compilation Group, 2020) of a 150-km swath west**
680 **of the trench. The blue horizontal line indicates the median uplift rate (0.22 mm/a). (C) Sediment thickness of trench-fill**
681 **deposits (red) (Bangs and Cande, 1997) and the distance of the trench from our terrace measurements (orange). Flat-slab**
682 **segments of the subducting Nazca plate are indicated for central Chile and Peru. (D) Maximum wave heights along the**
683 **WSC (light green) and the tidal range (dark green) between highest and lowest astronomical tides (Lorscheid and Rovere,**
684 **2019). (E) Precipitation (blue) along the WSC (Ceccherini et al., 2015) and azimuthal orientation of the coastline (cyan). (F)**
685 **Histogram of terrace-elevation measurements along the WSC.**

6. Conclusions

686

687 We measured 1,953 shoreline-angle elevations as proxies for paleo-sea levels of the MIS-5e and 5c terraces along
688 ~5,000 km of the WSC between Ecuador and Southern Chile. Our measurements are based on a systematic
689 methodology and the resulting data have been standardized within the framework of the WALIS database. Our
690 mapping was tied using referencing points based on previously published terrace-elevation estimates and age
691 constraints that are summarized in the compilation of Pedoja et al. (2014). The limitations of this database are
692 associated with the temporal accuracy and spatial distribution of the referencing points, which we attempt to consider
693 by providing a quality rating value to each measurement. The marine terrace elevations display a median value of 30.1
694 m for the MIS-5e level and a median uplift rate of 0.22 m/ka for MIS-5e and 5c. The lowest terrace elevations and
695 uplift rates along the entire South American margin occur immediately north of Concepción in Chile (6 m, 0.03 m/ka),
696 south of Chiclayo in northern Peru, and on the Santa Elena Peninsula in Ecuador (both 12 m, 0.07 m/ka). The regions
697 with exceptionally high marine terrace elevations ($\geq$ 100 m) comprise the Manta Peninsula in Ecuador, the San Juan
698 de Marcona area in south-central Peru, and three regions in south-central Chile (Topocalma, Carranza, and Arauco).

699 The pattern of terrace elevations displays short-, medium- and long-wavelength structures controlled by a combination
700 of various mechanisms. Long-wavelength structures may be controlled by deep-seated processes at the plate interface,
701 such as the subduction of major bathymetric anomalies (e.g. Manta Peninsula and San Juan de Marcona region). In
702 contrast, short-wavelength deformation patterns may be controlled by crustal faults rooted within the upper plate (e.g.,
703 between Mejillones and Valparaíso).

704 Latitudinal climate characteristics along the WSC may influence the generation and preservation of marine terraces.
705 An increase in wave height and tidal range generally results in enhanced erosion and morphologically well-expressed,
706 sharply defined marine terraces, which correlates with the southward increase in the number of our marine terrace
707 measurements. Conversely, river incision and lateral scouring in areas with high precipitation may degrade marine
708 terraces, thus decreasing the number of potential marine terrace measurements, such as observed south of Valparaíso.

709

728

7.   References

730   Anderson, R.S., Densmore, A.L., Ellis, M.A., 1999. The generation and degradation of marine terraces. Basin
731   Research 11(1), 7–19. doi:10.1046/j.1365-2117.1999.00085.x.

732   Angermann, D., Klotz, J., Reigber, C., 1999. Space-geodetic estimation of the Nazca-South America Euler vector.
733   Earth and Planetary Science Letters 171(3), 329–334. doi:10.1016/S0012-821X(99)00173-9.

734   Baker, A., Allmendinger, R.W., Owen, L.A., Rech, J.A., 2013. Permanent deformation caused by subduction
735   earthquakes in northern Chile. Nature Geoscience 6(6), 492–496. doi:10.1038/ngeo1789.

736   Bangs, N.L., Cande, S.C., 1997. Episodic development of a convergent margin inferred from structures and
737   processes along the southern Chile margin. Tectonics 16(3), 489–503.

738   Barazangi, M., Isacks, B.L., 1976. Spatial distribution of earthquakes and subduction of the Nazca plate beneath
739   South America. Geology 4(11), 686. doi:10.1130/0091-7613(1976)4<686:SDOEAS>2.0.CO;2.

740   Beck, S., Barrientos, S., Kausel, E., Reyes, M., 1998. Source characteristics of historic earthquakes along the central
741   Chile subduction zone. Journal of South American Earth Sciences 11(2), 115–129. doi:10.1016/S0895-
742   9811(98)00005-4.

743   Bendix, J., Rollenbeck, R., Reudenbach, C., 2006. Diurnal patterns of rainfall in a tropical Andean valley of
744   southern Ecuador as seen by a vertically pointing K-band Doppler radar. International Journal of Climatology
745   26(6), 829–846. doi:10.1002/joc.1267.

746   Bernhardt, A., Hebbeln, D., Regenberg, M., Lückge, A., Strecker, M.R., 2016. Shelfal sediment transport by an
747   undercurrent forces turbidity-current activity during high sea level along the Chile continental margin. Geology
748   44(4), 295–298. doi:10.1130/G37594.1.

749   Bernhardt, A., Schwanghart, W., Hebbeln, D., Stuut, J.-B.W., Strecker, M.R., 2017. Immediate propagation of
750   deglacial environmental change to deep-marine turbidite systems along the Chile convergent margin. Earth and
751   Planetary Science Letters 473, 190–204. doi:10.1016/j.epsl.2017.05.017.

752   Bilek, S.L., 2010. Invited review paper: Seismicity along the South American subduction zone: Review of large
753   earthquakes, tsunamis, and subduction zone complexity. Tectonophysics 495(1-2), 2–14.
754   doi:10.1016/j.tecto.2009.02.037.

755   Bilek, S.L., Schwartz, S.Y., DeShon, H.R., 2003. Control of seafloor roughness on earthquake rupture behavior.
756   Tectonics 31(5), 455. doi:10.1130/0091-7613(2003)031<0455:COSROE>2.0.CO;2.

Earth System
Science
Data

Open Access

Discussions

757 Binnie, A., Dunai, T.J., Binnie, S.A., Victor, P., González, G., Bolten, A., 2016. Accelerated late quaternary uplift
758   revealed by 10Be exposure dating of marine terraces, Mejillones Peninsula, northern Chile. Quaternary
759   Geochronology 36, 12–27. doi:10.1016/j.quageo.2016.06.005.

760 Bookhagen, B., Strecker, M.R., 2008. Orographic barriers, high-resolution TRMM rainfall, and relief variations
761   along the eastern Andes. Geophysical Research Letters 35(6), 139. doi:10.1029/2007GL032011.

762 Cahill, T., Isacks, B.L., 1992. Seismicity and shape of the subducted Nazca Plate. Journal of Geophysical Research
763   97(B12), 17503. doi:10.1029/92JB00493.

764 Ceccherini, G., Ameztoy, I., Hernández, C., Moreno, C., 2015. High-Resolution Precipitation Datasets in South
765   America and West Africa based on Satellite-Derived Rainfall, Enhanced Vegetation Index and Digital Elevation
766   Model. Remote Sensing 7(5), 6454–6488. doi:10.3390/rs70506454.

767 Cembrano, J., Lavenu, A., Yañez, G., Riquelme, R., García, M., González, G., Hérail, G., 2007. Neotectonics. In:
768   Moreno, T., Gibbons, W. (Eds.), The geology of Chile. Geological Society, London, pp. 231–261.

769 Clift, P., Vannucchi, P., 2004. Controls on tectonic accretion versus erosion in subduction zones: Implications for
770   the origin and recycling of the continental crust. Reviews of Geophysics 42(2), 19. doi:10.1029/2003RG000127.

771 Clift, P.D., Hartley, A.J., 2007. Slow rates of subduction erosion and coastal underplating along the Andean margin
772   of Chile and Peru. Geology 35(6), 503. doi:10.1130/G23584A.1.

773 Cloos, M., Shreve, R.L., 1988. Subduction-channel model of prism accretion, melange formation, sediment
774   subduction, and subduction erosion at convergent plate margins: 1. Background and description. Pure and
775   Applied Geophysics 128(3-4), 455–500. doi:10.1007/BF00874548.

776 Cloos, M., Shreve, R.L., 1996. Shear-zone thickness and the seismicity of Chilean- and Marianas-type subduction
777   zones. Geology 24(2), 107. doi:10.1130/0091-7613(1996)024<0107:SZTATS>2.3.CO;2.

778 Collot, J.-Y., Charvis, P., Gutscher, M.-A., Operto, S., 2002. Exploring the Ecuador-Colombia Active Margin and
779   Interplate Seismogenic Zone. Eos, Transactions, American Geophysical Union 83(17), 185.
780   doi:10.1029/2002EO000120.

781 Collot, J.-Y., Sanclemente, E., Nocquet, J.-M., Leprêtre, A., Ribodetti, A., Jarrin, P., Chlieh, M., Graindorge, D.,
782   Charvis, P., 2017. Subducted oceanic relief locks the shallow megathrust in central Ecuador. Journal of
783   Geophysical Research: Solid Earth 122(5), 3286–3305. doi:10.1002/2016JB013849.

784 Costa, C., Machette, M.N., Dart, R.L., Bastias, H.E., Paredes, J.D., Perucca, L.P., Tello, G.E., Haller, K.M., 2000.
785   Map and database of Quaternary faults and folds in Argentina. Open-File Report. US Geological Survey.
786   http://dx.doi.org/10.3133/ofr00108.

787   Coudurier-Curveur, A., Lacassin, R., Armijo, R., 2015. Andean growth and monsoon winds drive landscape
788   evolution at SW margin of South America. Earth and Planetary Science Letters 414, 87–99.
789   doi:10.1016/j.epsl.2014.12.047.

790   DeMets, C., Gordon, R.G., Argus, D.F., 2010. Geologically current plate motions. Geophysical Journal International
791   181(1), 1–80. doi:10.1111/j.1365-246X.2009.04491.x.

792   Espurt, N., Funiciello, F., Martinod, J., Guillaume, B., Regard, V., Faccenna, C., Brusset, S., 2008. Flat subduction
793   dynamics and deformation of the South American plate: Insights from analog modeling. Tectonics 27(3), n/a-
794   n/a. doi:10.1029/2007TC002175.

795   Freisleben, R., Jara-Muñoz, J., Melnick, D., Martínez, J.M., Strecker, M., 2020. Marine terraces of the last
796   interglacial period along the Pacific coast of South America (1°N-40°S). Zenodo.
797   doi:10.5281/ZENODO.4309748.

798   Fryer, P., Smoot, N.C., 1985. Processes of seamount subduction in the Mariana and Izu-Bonin trenches. Marine
799   Geology 64(1-2), 77–90. doi:10.1016/0025-3227(85)90161-6.

800   Fuenzalida, H., Cooke, R., Paskoff, R., Segerstrom, K., Weischet, W., 1965. High Stands of Quaternary Sea Level
801   Along the Chilean Coast. Geological Society of America Special Papers 84, 473–496.

802   Gallen, S.F., Wegmann, K.W., Bohnenstiehl, D.R., Pazzaglia, F.J., Brandon, M.T., Fassoulas, C., 2014. Active
803   simultaneous uplift and margin-normal extension in a forearc high, Crete, Greece. Earth and Planetary Science
804   Letters 398, 11–24. doi:10.1016/j.epsl.2014.04.038.

805   Gardner, T.W., Fisher, D.M., Morell, K.D., Cupper, M.L., 2013. Upper-plate deformation in response to flat slab
806   subduction inboard of the aseismic Cocos Ridge, Osa Peninsula, Costa Rica. Lithosphere 5(3), 247–264.
807   doi:10.1130/L251.1.

808   Garreaud, R.D., 2009. The Andes climate and weather. Advances in Geosciences 22, 3–11. doi:10.5194/adgeo-22-3-
809   2009.

810   GEBCO Bathymetric Compilation Group, 2020. The GEBCO_2020 Grid - a continuous terrain model of the global
811   oceans and land. British Oceanographic Data Centre, National Oceanography Centre, NERC, UK.

812   Geersen, J., Ranero, C.R., Barckhausen, U., Reichert, C., 2015. Subducting seamounts control interplate coupling
813   and seismic rupture in the 2014 Iquique earthquake area. Nature communications 6, 8267.
814   doi:10.1038/ncomms9267.

815   German Aerospace Center (DLR), 2018. TanDEM-X - Digital Elevation Model (DEM) - Global, 12m.

816   González, G., Carrizo, D., 2003. Segmentación, cinemática y cronología relativa de la deformación tardía de la Falla
817   Salar del Carmen, Sistema de Fallas de Atacama, (23°40'S), norte de Chile. Revista Geológica de Chile 30(2).
818   doi:10.4067/S0716-02082003000200005.

819   Gutscher, M.-A., Malavieille, J., Lallemand, S., Collot, J.-Y., 1999. Tectonic segmentation of the North Andean
820   margin: impact of the Carnegie Ridge collision. Earth and Planetary Science Letters 168(3-4), 255–270.
821   doi:10.1016/S0012-821X(99)00060-6.

822   Gutscher, M.-A., Spakman, W., Bijwaard, H., Engdahl, E.R., 2000. Geodynamics of flat subduction: Seismicity and
823   tomographic constraints from the Andean margin. Tectonics 19(5), 814–833. doi:10.1029/1999TC001152.

824   Hampel, A., 2002. The migration history of the Nazca Ridge along the Peruvian active margin: a re-evaluation.
825   Earth and Planetary Science Letters 203(2), 665–679. doi:10.1016/S0012-821X(02)00859-2.

826   Hayes, G.P., Moore, G.L., Portner, D.E., Hearne, M., Flamme, H., Furtney, M., Smoczyk, G.M., 2018. Slab2, a
827   comprehensive subduction zone geometry model. Science (New York, N.Y.) 362(6410), 58–61.
828   doi:10.1126/science.aat4723.

829   Hearty, P.J., Hollin, J.T., Neumann, A.C., O'Leary, M.J., McCulloch, M., 2007. Global sea-level fluctuations during
830   the Last Interglaciation (MIS 5e). Quaternary Science Reviews 26(17-18), 2090–2112.
831   doi:10.1016/j.quascirev.2007.06.019.

832   Hilde, T.W.C., 1983. Sediment subduction versus accretion around the pacific. Tectonophysics 99(2-4), 381–397.
833   doi:10.1016/0040-1951(83)90114-2.

834   Houston, J., Hartley, A.J., 2003. The central Andean west-slope rainshadow and its potential contribution to the
835   origin of hyper-aridity in the Atacama Desert. International Journal of Climatology 23(12), 1453–1464.
836   doi:10.1002/joc.938.

837   Hsu, J.T., 1992. Quaternary uplift of the Peruvian coast related to the subduction of the Nazca Ridge: 13.5 to 15.6
838   degrees south latitude. Quaternary International 15-16, 87–97. doi:10.1016/1040-6182(92)90038-4.

839   Hsu, J.T., Leonard, E.M., Wehmiller, J.F., 1989. Aminostratigraphy of Peruvian and Chilean Quaternary marine
840   terraces. Quaternary Science Reviews 8(3), 255–262. doi:10.1016/0277-3791(89)90040-1.

841   Huene, R. von, Pecher, I.A., Gutscher, M.-A., 1996. Development of the accretionary prism along Peru and material
842   flux after subduction of Nazca Ridge. Tectonics 15(1), 19–33. doi:10.1029/95TC02618.

843   Jaillard, E., Hérail, G., Monfret, T., Díaz-Martínez, E., Baby, P., Lavenu, A., Dumont, J.F., 2000. Tectonic evolution
844   of the Andes of Ecuador, Peru, Bolivia, and northernmost Chile. In: Cordani, U.G., Milani, E.J., Thomaz, F.A.,
845   Campos, D.A. (Eds.), Tectonic evolution of South America. Sociedad Brasileira de Geologia, Rio de Janeiro,
846   pp. 481–559.

847   Jara-Muñoz, J., Melnick, D., Brill, D., Strecker, M.R., 2015. Segmentation of the 2010 Maule Chile earthquake
848   rupture from a joint analysis of uplifted marine terraces and seismic-cycle deformation patterns. Quaternary
849   Science Reviews 113, 171–192. doi:10.1016/j.quascirev.2015.01.005.

850   Jara-Muñoz, J., Melnick, D., Socquet, A., Cortés-Aranda, J., Strecker, M.R., 2018. Slip rate and earthquake
851   recurrence of the Pichilemu Fault. Congreso Geológico Chileno, 15th.

852   Jara-Muñoz, J., Melnick, D., Strecker, M.R., 2016. TerraceM: A MATLAB® tool to analyze marine and lacustrine
853   terraces using high-resolution topography. Geosphere 12(1), 176–195. doi:10.1130/GES01208.1.

854   Jara-Muñoz, J., Melnick, D., Zambrano, P., Rietbrock, A., González, J., Argandoña, B., Strecker, M.R., 2017.
855   Quantifying offshore fore-arc deformation and splay-fault slip using drowned Pleistocene shorelines, Arauco
856   Bay, Chile. Journal of Geophysical Research: Solid Earth 122(6), 4529–4558. doi:10.1002/2016JB013339.

857   Jordan, T.E., Isacks, B.L., Allmendinger, R.W., Brewer, J.A.O.N., Ramos, V.A., Ando, C.J., 1983. Andean tectonics
858   related to geometry of subducted Nazca plate. Geological Society of America Bulletin 94(3), 341.
859   doi:10.1130/0016-7606(1983)94<341:ATRTGO>2.0.CO;2.

860   Kay, S.M., Maksaev, V., Moscoso, R., Mpodozis, C., Nasi, C., 1987. Probing the evolving Andean Lithosphere:
861   Mid-Late Tertiary magmatism in Chile (29°–30°30′S) over the modern zone of subhorizontal subduction.
862   Journal of Geophysical Research 92(B7), 6173. doi:10.1029/JB092iB07p06173.

863   Lajoie, K.R., 1986. Coastal tectonics. In: Wallace, R.E. (Ed.), Active tectonics. National Academics Press,
864   Washington D.C., pp. 95–124.

865   Lamb, S., Davis, P., 2003. Cenozoic climate change as a possible cause for the rise of the Andes. Nature 425(6960),
866   792–797. doi:10.1038/nature02049.

867   Lohrmann, J., Kukowski, N., Adam, J., Oncken, O., 2003. The impact of analogue material properties on the
868   geometry, kinematics, and dynamics of convergent sand wedges. Journal of Structural Geology 25(10), 1691–
869   1711. doi:10.1016/S0191-8141(03)00005-1.

870   Lorscheid, T., Rovere, A., 2019. The indicative meaning calculator – quantification of paleo sea-level relationships
871   by using global wave and tide datasets. Open Geospatial Data, Software and Standards 4(1), 591.
872   doi:10.1186/s40965-019-0069-8.

873   Macharé, J., Ortlieb, L., 1992. Plio-Quaternary vertical motions and the subduction of the Nazca Ridge, central coast
874   of Peru. Tectonophysics 205(1-3), 97–108. doi:10.1016/0040-1951(92)90420-B.

875   Maldonado, V., Contreras, M., Melnick, D., 2020. A comprehensive database of active and potentially-active
876   continental faults in Chile at 1:25,000 scale: scientific data. PANGAEA - Data Publisher for Earth &
877   Environmental Science (in press).

878   Manea, V.C., Pérez-Gussinyé, M., Manea, M., 2012. Chilean flat slab subduction controlled by overriding plate
879   thickness and trench rollback. Geology 40(1), 35–38. doi:10.1130/G32543.1.

880   Mann, P., Taylor, F.W., Lagoe, M.B., Quarles, A., Burr, G., 1998. Accelerating late Quaternary uplift of the New
881   Georgia Island Group (Solomon island arc) in response to subduction of the recently active Woodlark spreading
882   center and Coleman seamount. Tectonophysics 295(3-4), 259–306. doi:10.1016/S0040-1951(98)00129-2.

883   Marcaillou, B., Collot, J.-Y., Ribodetti, A., d'Acremont, E., Mahamat, A.-A., Alvarado, A., 2016. Seamount
884   subduction at the North-Ecuadorian convergent margin: Effects on structures, inter-seismic coupling and
885   seismogenesis. Earth and Planetary Science Letters 433, 146–158. doi:10.1016/j.epsl.2015.10.043.

886   Martinod, J., Regard, V., Letourmy, Y., Henry, H., Hassani, R., Baratchart, S., Carretier, S., 2016a. How do
887   subduction processes contribute to forearc Andean uplift? Insights from numerical models. Journal of
888   Geodynamics 96, 6–18. doi:10.1016/j.jog.2015.04.001.

889   Martinod, J., Regard, V., Riquelme, R., Aguilar, G., Guillaume, B., Carretier, S., Cortés-Aranda, J., Leanni, L.,
890   Hérail, G., 2016b. Pleistocene uplift, climate and morphological segmentation of the Northern Chile coasts
891   (24°S–32°S): Insights from cosmogenic 10Be dating of paleoshorelines. Geomorphology 274, 78–91.
892   doi:10.1016/j.geomorph.2016.09.010.

893   Melet, A., Teatini, P., Le Cozannet, G., Jamet, C., Conversi, A., Benveniste, J., Almar, R., 2020. Earth Observations
894   for Monitoring Marine Coastal Hazards and Their Drivers. Surveys in Geophysics 41(6), 1489–1534.
895   doi:10.1007/s10712-020-09594-5.

896   Melnick, D., 2016. Rise of the central Andean coast by earthquakes straddling the Moho. Nature Geoscience 9(5),
897   401–407. doi:10.1038/ngeo2683.

898   Melnick, D., Bookhagen, B., Echtler, H.P., Strecker, M.R., 2006. Coastal deformation and great subduction
899   earthquakes, Isla Santa Maria, Chile (37°S). Geological Society of America Bulletin 118(11-12), 1463–1480.
900   doi:10.1130/B25865.1.

901   Melnick, D., Bookhagen, B., Strecker, M.R., Echtler, H.P., 2009. Segmentation of megathrust rupture zones from
902   fore-arc deformation patterns over hundreds to millions of years, Arauco peninsula, Chile. Journal of
903   Geophysical Research: Solid Earth 114(B1), 6140. doi:10.1029/2008JB005788.

904   Melnick, D., Hillemann, C., Jara-Muñoz, J., Garrett, E., Cortés-Aranda, J., Molina, D., Tassara, A., Strecker, M.R.,
905   2019. Hidden Holocene slip along the coastal El Yolki Fault in Central Chile and its possible link with
906   megathrust earthquakes. Journal of Geophysical Research: Solid Earth 124(7), 7280–7302.
907   doi:10.1029/2018JB017188.

908   Melnick, D., Maldonado, V., Contreras, M., 2020. Database of active and potentially-active continental faults in
909   Chile at 1:25,000 scale. PANGAEA - Data Publisher for Earth & Environmental Science.
910   doi:10.1594/PANGAEA.922241.

911   Melosh, H.J., Raefsky, A., 1980. The dynamical origin of subduction zone topography. Geophysical Journal
912   International 60(3), 333–354. doi:10.1111/j.1365-246X.1980.tb04812.x.

Earth System
Science
Data

Open Access

Discussions

913   Menant, A., Angiboust, S., Gerya, T., Lacassin, R., Simoes, M., Grandin, R., 2020. Transient stripping of
914   subducting slabs controls periodic forearc uplift. Nature communications 11(1), 1823. doi:10.1038/s41467-020-
915   15580-7.

916   Morgan, J.K., Bangs, N.L., 2017. Recognizing seamount-forearc collisions at accretionary margins: Insights from
917   discrete numerical simulations. Geology 45(7), 635–638. doi:10.1130/G38923.1.

918   Müller, R.D., Sdrolias, M., Gaina, C., Roest, W.R., 2008. Age, spreading rates, and spreading asymmetry of the
919   world's ocean crust. Geochemistry, Geophysics, Geosystems 9(4). doi:10.1029/2007GC001743.

920   Naranjo, J.A., 1987. Interpretacion de la actividad cenozoica superior a lo largo de la Zona de Falla Atacama, Norte
921   de Chile. Revista Geológica de Chile(31), 43–55.

922   Ortlieb, L., Macharé, J., 1990. Geochronologia y morfoestratigrafia de terrazas marinas del Pleistoceno superior: El
923   caso de San Juan-Marcona, Peru. Boletín de la Sociedad Geológica del Perú 81, 87–106.

924   Ortlieb, L., Zazo, C., Goy, J.L., Dabrio, C., Macharé, J., 1996. Pampa del Palo: an anomalous composite marine
925   terrace on the uprising coast of southern Peru. Journal of South American Earth Sciences 9(5-6), 367–379.
926   doi:10.1016/S0895-9811(96)00020-X.

927   Ota, Y., Miyauchi, T., Paskoff, R., Koba, M., 1995. Plio-Quaternary marine terraces and their deformation along the
928   Altos de Talinay, North-Central Chile. Revista Geológica de Chile 22(1), 89–102.

929   Paris, P.J., Walsh, J.P., Corbett, D.R., 2016. Where the continent ends. Geophysical Research Letters 43(23),
930   12,208-12,216. doi:10.1002/2016GL071130.

931   Pedoja, K., Dumont, J.F., Lamothe, M., Ortlieb, L., Collot, J.-Y., Ghaleb, B., Auclair, M., Alvarez, V., Labrousse,
932   B., 2006a. Plio-Quaternary uplift of the Manta Peninsula and La Plata Island and the subduction of the Carnegie
933   Ridge, central coast of Ecuador. Journal of South American Earth Sciences 22(1-2), 1–21.
934   doi:10.1016/j.jsames.2006.08.003.

935   Pedoja, K., Husson, L., Johnson, M.E., Melnick, D., Witt, C., Pochat, S., Nexer, M., Delcaillau, B., Pinegina, T.,
936   Poprawski, Y., Authemayou, C., Elliot, M., Regard, V., Garestier, F., 2014. Coastal staircase sequences
937   reflecting sea-level oscillations and tectonic uplift during the Quaternary and Neogene. Earth-Science Reviews
938   132, 13–38. doi:10.1016/j.earscirev.2014.01.007.

939   Pedoja, K., Ortlieb, L., Dumont, J.F., Lamothe, M., Ghaleb, B., Auclair, M., Labrousse, B., 2006b. Quaternary
940   coastal uplift along the Talara Arc (Ecuador, Northern Peru) from new marine terrace data. Marine Geology
941   228(1-4), 73–91. doi:10.1016/j.margeo.2006.01.004.

942   Pilger, R.H., 1981. Plate reconstructions, aseismic ridges, and low-angle subduction beneath the Andes. Geological
943   Society of America Bulletin 92(7), 448. doi:10.1130/0016-7606(1981)92<448:PRARAL>2.0.CO;2.

944 Ramos, V.A., Folguera, A., 2009. Andean flat-slab subduction through time. Geological Society, London, Special
945   Publications 327(1), 31–54. doi:10.1144/SP327.3.

946 Regard, V., Saillard, M., Martinod, J., Audin, L., Carretier, S., Pedoja, K., Riquelme, R., Paredes, P., Hérail, G.,
947   2010. Renewed uplift of the Central Andes Forearc revealed by coastal evolution during the Quaternary. Earth
948   and Planetary Science Letters 297(1-2), 199–210. doi:10.1016/j.epsl.2010.06.020.

949 Rehak, K., Bookhagen, B., Strecker, M.R., Echtler, H.P., 2010. The topographic imprint of a transient climate
950   episode: the western Andean flank between 15.5° and 41.5°S. Earth Surface Processes and Landforms 35(13),
951   1516–1534. doi:10.1002/esp.1992.

952 Rodríguez, M.P., Carretier, S., Charrier, R., Saillard, M., Regard, V., Hérail, G., Hall, S., Farber, D., Audin, L.,
953   2013. Geochronology of pediments and marine terraces in north-central Chile and their implications for
954   Quaternary uplift in the Western Andes. Geomorphology 180-181, 33–46.
955   doi:10.1016/j.geomorph.2012.09.003.

956 Rohling, E.J., Grant, K., Bolshaw, M., Roberts, A.P., Siddall, M., Hemleben, C., Kucera, M., 2009. Antarctic
957   temperature and global sea level closely coupled over the past five glacial cycles. Nature Geoscience 2(7), 500–
958   504. doi:10.1038/ngeo557.

959 Rovere, A., Ryan, D., Murray-Wallace, C., Simms, A., Vacchi, M., Dutton, A., Lorscheid, T., Chutcharavan, P.,
960   Brill, D., Bartz, M., Jankowski, N., Mueller, D., Cohen, K., Gowan, E., 2020. Descriptions of database fields for
961   the World Atlas of Last Interglacial Shorelines (WALIS). Zenodo. doi:10.5281/ZENODO.3961544.

962 Ruh, J.B., Sallarès, V., Ranero, C.R., Gerya, T., 2016. Crustal deformation dynamics and stress evolution during
963   seamount subduction: High-resolution 3-D numerical modeling. Journal of Geophysical Research: Solid Earth
964   121(9), 6880–6902. doi:10.1002/2016JB013250.

965 Saillard, M., 2008. Dynamique du soulèvement côtier Pléistocène des Andes centrales Etude de l'évolution
966   géomorphologique et datations (10Be) de séquences de terrasses marines (Sud Pérou - Nord Chili), Université
967   Paul Sabatier, Toulouse.

968 Saillard, M., Hall, S.R., Audin, L., Farber, D.L., Hérail, G., Martinod, J., Regard, V., Finkel, R.C., Bondoux, F.,
969   2009. Non-steady long-term uplift rates and Pleistocene marine terrace development along the Andean margin
970   of Chile (31°S) inferred from 10Be dating. Earth and Planetary Science Letters 277(1-2), 50–63.
971   doi:10.1016/j.epsl.2008.09.039.

972 Saillard, M., Hall, S.R., Audin, L., Farber, D.L., Regard, V., Hérail, G., 2011. Andean coastal uplift and active
973   tectonics in southern Peru: 10Be surface exposure dating of differentially uplifted marine terrace sequences (San
974   Juan de Marcona, ~15.4°S). Geomorphology 128(3-4), 178–190. doi:10.1016/j.geomorph.2011.01.004.

975   Santibáñez, I., Cembrano, J., García-Pérez, T., Costa, C., Yáñez, G., Marquardt, C., Arancibia, G., González, G.,
976   2019. Crustal faults in the Chilean Andes: geological constraints and seismic potential. Andean Geology 46(1),
977   32. doi:10.5027/andgeoV46n1-3067.

978   Scholl, D.W., Huene, R. von, 2007. Crustal recycling at modern subduction zones applied to the past—Issues of
979   growth and preservation of continental basement crust, mantle geochemistry, and supercontinent reconstruction.
980   In: 4-D Framework of Continental Crust. Geological Society of America, pp. 9–32.

981   Schwanghart, W., Kuhn, N.J., 2010. TopoToolbox: A set of Matlab functions for topographic analysis.
982   Environmental Modelling & Software 25(6), 770–781. doi:10.1016/j.envsoft.2009.12.002.

983   Schweller, W.J., Kulm, L.D., Prince, R.A., 1981. Tectonics, structure, and sedimentary framework of the Peru-Chile
984   Trench. Geological Society of America Memoir 154, 323–350. doi:10.1130/MEM154-p323.

985   Shackleton, N.J., Sánchez-Goñi, M.F., Pailler, D., Lancelot, Y., 2003. Marine Isotope Substage 5e and the Eemian
986   Interglacial. Global and Planetary Change 36(3), 151–155. doi:10.1016/S0921-8181(02)00181-9.

987   Siddall, M., Chappell, J., Potter, E.-K., 2006. Eustatic sea level during past interglacials. In: Sirocko, F., Litt, T.,
988   Claussen, M., Sanchez-Goni, M.-F. (Eds.), The climate of past interglacials. Elsevier, Amsterdam, pp. 75–92.

989   Sobolev, S.V., Babeyko, A.Y., 2005. What drives orogeny in the Andes? Geology 33(8), 617–620.
990   doi:10.1130/G21557AR.1.

991   Stern, C.R., 1991. Role of subduction erosion in the generation of Andean magmas. Geology 19(1), 78.
992   doi:10.1130/0091-7613(1991)019<0078:ROSEIT>2.3.CO;2.

993   Stirling, C.H., Esat, T.M., Lambeck, K., McCulloch, M.T., 1998. Timing and duration of the Last Interglacial:
994   evidence for a restricted interval of widespread coral reef growth. Earth and Planetary Science Letters 160(3-4),
995   745–762. doi:10.1016/S0012-821X(98)00125-3.

996   Strecker, M.R., Alonso, R.N., Bookhagen, B., Carrapa, B., Hilley, G.E., Sobel, E.R., Trauth, M.H., 2007. Tectonics
997   and Climate of the Southern Central Andes. Annual Review of Earth and Planetary Sciences 35(1), 747–787.
998   doi:10.1146/annurev.earth.35.031306.140158.

999   Suárez, G., Molnar, P., Burchfiel, B.C., 1983. Seismicity, fault plane solutions, depth of faulting, and active
1000   tectonics of the Andes of Peru, Ecuador, and southern Colombia. Journal of Geophysical Research 88(B12),
1001   10403–10428. doi:10.1029/JB088iB12p10403.

1002   Taylor, F.W., Frohlich, C., Lecolle, J., Strecker, M., 1987. Analysis of partially emerged corals and reef terraces in
1003   the central Vanuatu Arc: Comparison of contemporary coseismic and nonseismic with quaternary vertical
1004   movements. Journal of Geophysical Research 92(B6), 4905. doi:10.1029/JB092iB06p04905.

1005   Veloza, G., Styron, R., Taylor, M., Mora, A., 2012. Open-source archive of active faults for northwest South
1006   America. GSA Today 22(10), 4–10. doi:10.1130/GSAT-G156A.1.

1007   Venzke, E., 2013. Volcanoes of the World, v. 4.3.4. Global Volcanism Program.

1008   Victor, P., Sobiesiak, M., Glodny, J., Nielsen, S.N., Oncken, O., 2011. Long-term persistence of subduction
1009   earthquake segment boundaries: Evidence from Mejillones Peninsula, northern Chile. Journal of Geophysical
1010   Research 116(B2), 93. doi:10.1029/2010JB007771.

1011   Villegas-Lanza, J.C., Chlieh, M., Cavalié, O., Tavera, H., Baby, P., Chire-Chira, J., Nocquet, J.-M., 2016. Active
1012   tectonics of Peru: Heterogeneous interseismic coupling along the Nazca megathrust, rigid motion of the
1013   Peruvian Sliver, and Subandean shortening accommodation. Journal of Geophysical Research: Solid Earth
1014   121(10), 7371–7394. doi:10.1002/2016JB013080.

1015   von Huene, R., Corvalán, J., Flueh, E.R., Hinz, K., Korstgard, J., Ranero, C.R., Weinrebe, W., 1997. Tectonic
1016   control of the subducting Juan Fernández Ridge on the Andean margin near Valparaiso, Chile. Tectonics 16(3),
1017   474–488. doi:10.1029/96TC03703.

1018   von Huene, R., Scholl, D.W., 1991. Observations at convergent margins concerning sediment subduction,
1019   subduction erosion, and the growth of continental crust. Geology 29(3), 279. doi:10.1029/91RG00969.

1020   Wang, K., Bilek, S.L., 2011. Do subducting seamounts generate or stop large earthquakes? Geology 39(9), 819–822.
1021   doi:10.1130/G31856.1.

1022   Wang, K., Bilek, S.L., 2014. Invited review paper: Fault creep caused by subduction of rough seafloor relief.
1023   Tectonophysics 610, 1–24. doi:10.1016/j.tecto.2013.11.024.

1024   Watts, A.B., Daly, S.F., 1981. Long Wavelength Gravity and Topography Anomalies. Annual Review of Earth and
1025   Planetary Sciences 9, 415–448.

1026